Univerzita Karlova v Praze
Matematicko-fyzikální fakulta

DIPLOMOVÁ PRÁCE

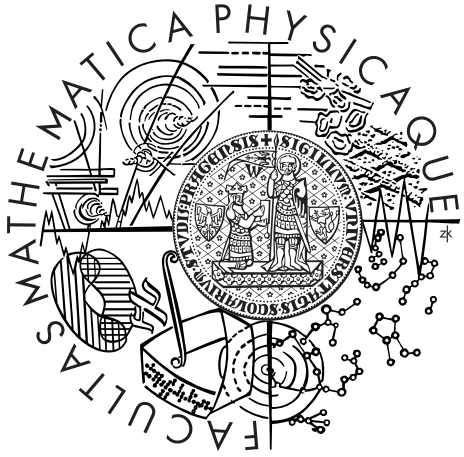

Bc. Jan Moudřík

Kooperativní jevy v cerových sloučeninách na hranici magnetismu

Katedra fyziky kondenzovaných látek

Vedoucí diplomové práce: RNDr. Jan Prokleška, Ph.D.

Studijní program: Fyzika (N1701)
Studijní obor: FKSM (1701T041)

Praha 2015

Charles University in Prague
Faculty of Mathematics and Physics

MASTER THESIS

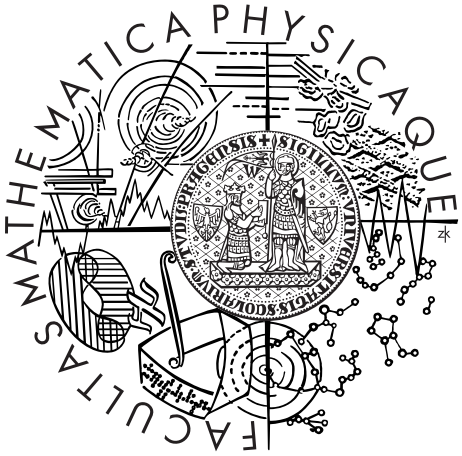

Bc. Jan Moudřík

Cooperative phenomena in cerium compounds on the verge of magnetism

Department of Condensed Matter Physics

Supervisor of the master thesis: RNDr. Jan Prokleška, Ph.D.
Study programme: Fyzika (N1701)
Specialization: FKSM (1701T041)

Prague 2015

Foremostly, I would like to thank RNDr. Jan Prokleška, Ph.D. for numerous revisions and consultations as well as his kind and patient support throughout my whole Bachelor's and Master's studies. The presented work would also not be possible without the support of our many collaborators, I would thus like to thank RNDr. Jiří Pospíšil, Ph.D., RNDr. Ivana Císařová, CSc., RNDr. Milan Klicpera, Dr. Bachir Ouladdiaf, prof. Alexander Andreev, DrSc., Denis Gorbunov and prof. RNDr. Vladimír Sechovský, DrSc. for their scientific help and advice. Experiments were performed in MLTL which is supported within the program of Czech Research Infrastructures (project no. LM2011025) and the work is a part of research project LG14037 financed by the Ministry of Education, Youth and Sports, Czech Republic. Last but not least, I would very much like to thank my partner, brother, parents and friends for their tireless love and support.

I declare that I carried out this master thesis independently, and only with the cited sources, literature and other professional sources.

I understand that my work relates to the rights and obligations under the Act No. 121/2000 Coll., the Copyright Act, as amended, in particular the fact that the Charles University in Prague has the right to conclude a license agreement on the use of this work as a school work pursuant to Section 60 paragraph 1 of the Copyright Act.

In ..... date ..... signature of the author

Název práce: Kooperativní jevy v cerových sloučeninách na hranici magnetismu

Autor: Bc. Jan Moudřík

Katedra: Katedra fyziky kondenzovaných látek

Vedoucí diplomové práce: RNDr. Jan Prokleška, Ph.D.

Abstrakt: V předkládané práci prezentujeme výsledky studia fyzikálních vlastností nové sloučeniny $CeCo_{0.715}Si_{2.285}$. Tato sloučenina krystalizuje v *I-4m2* struktuře s extrémně prodlouženou elementární buňkou (a = 4,13Å , c = 32,84Å) obsahující části $BaAl_4$ struktury. V nulovém magnetickém poli se sloučenina uspořádává antiferomagneticky při teplotě T_N = 10,0K. Za aplikace malých magnetických polí ($B < 0{,}5$T) podél osy c pozorujeme velké množství přechodů v magnetizaci – podobné chování je pozorované u tzv. „devil's staircase" systémů (např. CeSb, $CeCoGe_3$). Magnetizace zůstává víceméně konstantní v polích 1T až 45T za aplikace pole podél osy c, ale je ve srovnání s hodnotou očekávanou pro volný Ce^{3+} iont velice redukována ($0{,}3\mu_B$/Ce). Při aplikaci pole podél osy a pozorujeme chování typické pro nesnadnou osu magnetizace u materiálu s jednoosou anisotropií. Výsledky prvních neutronových difrakčních experimentů neumožnily úplné určení magnetické struktury.

Klíčová slova: Cerové sloučeniny, supravodivost, magnetismus

Title: Cooperative phenomena in cerium compounds on the verge of magnetism

Author: Bc. Jan Moudřík

Department: Department of Condensed Matter Physics

Supervisor: RNDr. Jan Prokleška, Ph.D.

Abstract: This work reports on physical properties of a novel $CeCo_{0.715}Si_{2.285}$ compound. The compound crystallizes in the *I-4m2* space group structure with extremely elongated unit cell ($a = 4.13$Å , $c = 32.84$Å) containing $BaAl_4$ structural patterns. In zero magnetic field it orders antiferromagnetically at $T_N = 10.0$K. Under application of magnetic field along the c-axis it manifests numerous magnetic transitions in small fields ($B < 0.5$T), resembling the so-called 'devil's staircase' behaviour (e.g. CeSb, $CeCoGe_3$). The magnetization is almost constant from 1T up to 45T for $H||c$ but considerably reduced ($0.3\mu_B$/Ce) with respect to the free Ce^{3+} ion. For fields applied along the a-axis typical behaviour for a hard axis in a material with uniaxial anisotropy is observed. The performed single crystal neutron diffraction experiment did not allow complete determination of magnetic structure.

Keywords: Cerium compounds, superconductivity, magnetism

Contents

Introduction

Understanding of magnetism, superconductivity and the underlying physical mechanisms is one of the big goals of basic condensed matter physics research. Such basic research might in the long-term bring applications like new magnetic memories such as (in the past) the MRAM architectures based on Giant Magnetoresistance (GMR, The Nobel Prize in Physics 2007 [1]).

Cerium compounds are very suitable candidates for such basic research studies which try to explain the physics behind various phenomena related to magnetism and superconductivity. Being f-electron systems, they exhibit a variety of interesting properties such as valence fluctuations, spin orderings, heavy fermions formation or anisotropic superconductivity. The competition between the Ruderman-Kittel-Kasuya-Yosida (RKKY) interaction and the Kondo effect plays a crucial role in these compounds. While the RKKY enhances long-range magnetic order – the f electrons are treated as localized with an indirect f-f interaction – the Kondo effect quenches the magnetic moments and leads to a heavy fermion state [2].

Cerium systems also display a number of curious superconducting phenomena as, for example, reentrant superconductivity ($Ce_{1-x}La_xAl_2$, [3, 4]), coexistence of superconductivity and magnetism ($Ce_{1-x}Gd_xRu_2$, [5]) or superconductivity in heavy-fermion systems ($CeCu_2Si_2$, [6]). For a very detailed overview of superconducting phases of f-electron compounds see Ref. [7]. Understanding these cooperative phenomena is fundamental to the above–mentioned proper understanding of physics of magnetism and superconductivity.

In the presented study we give an overview of the physical behaviour of a novel compound $CeCo_{0.715}Si_{2.285}$. The compound exhibits some very interesting magnetic behaviour which can be seen in other cerium based compounds but is not at all common. Its behaviour was published for the first time within the course of this study in Ref. [8]. The novelty of this compound has meant that its description and an attempt at a characterization of the underlying physical mechanism required quite an extensive study of its crystal and magnetic structure, specific heat, magnetization and resistivity dependence on temperature, magnetic field and pressure.

Originally, our aim was to study the CeTX_3 group of compounds (T and X denote a transition metal and Si/Ge, respectively) but during the various crystal growths we managed to grow the (then unknown) $CeCo_{0.715}Si_{2.285}$. Its characterization has showed some very curious and interesting behaviour and we have therefore decided to further focus mainly on its investigation.

Firstly, its crystal structure is interesting since the unit cell is extremely elongated ($a = b = 4.13$Å , $c = 32.84$Å) and contains patterns which are visible in the structure of the CeTX_3 group. Secondly, among other effects, its magnetic behaviour resembles that of the so-called 'devil's staircase' systems (e.g. CeSb [9], $CeCoGe_3$ [10]) and the consequently arising complex magnetic phase diagram is quite unusual as well.

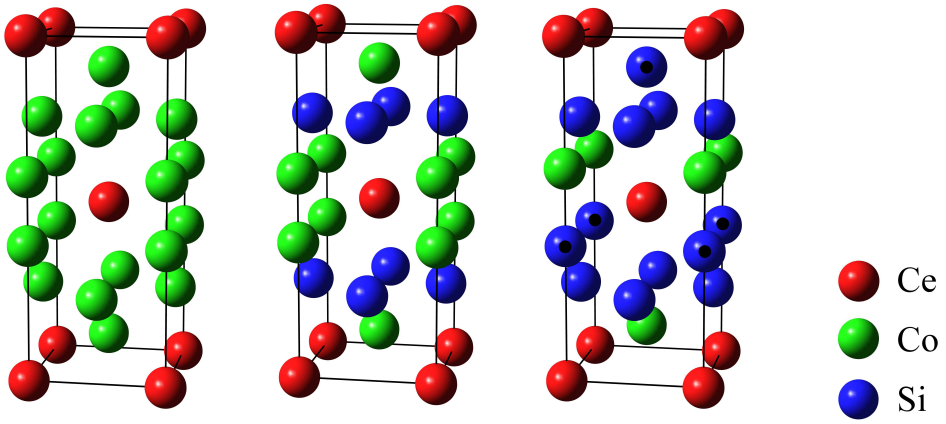

(a) (b) (c)

Figure 1: (a) $BaAl_4$ structure and its two derivatives (b) $ThCr_2Si_2$ and (c) $BaNiSn_3$.

Ternary Ce-based Compounds

As mentioned above, the structure of the $CeCo_{0.715}Si_{2.285}$ includes certain structural patterns observed in other ternary cerium based compounds and its behaviour is comparable to that of $CeCoGe_3$. It is therefore helpful to firstly familiarize ourself with this group of compounds.

Most of $CeTX_3$ compounds crystallize in the tetragonal $BaNiSn_3$-type structure, specifically the series $CeTSi_3$ (T: Co, Ru, Rh, Pd, Os, Ir, Pt) and $CeTGe_3$ (T: Fe, Co, Rh, Ir)[11]. The lattice parameters of the compounds of the two series do not vary very much, 4.1Å $\leq a \leq$ 4.4Å and 9.5Å $\leq c \leq$ 10.0Å. The $BaNiSn_3$ structure can be seen as being derived from the $BaAl_4$ structure, another later relevant structure derived from $BaAl_4$ is the $ThCr_2Si_2$ structure in which some heavy fermion superconductors crystallize, e.g. $CeRh_2Si_2$ [12] or $CeCu_2Si_2$ [6]. Figure 1 shows the mentioned structures. The $ThCr_2Si_2$ structure is centrosymmetric while the $BaNiSn_3$ is not. This fact makes the whole group quite interesting since $CeRhSi_3$ [11], $CeIrSi_3$ [13], $CeCoGe_3$ [14] and $CeIrGe_3$ [15] are pressure-induced superconductors.[1] A typical $CeTX_3$ temperature-pressure phase diagram is similar to that of $CeIrSi_3$ – with increasing pressure the ordering temperature decreases (generally non-monotonously) and at a certain critical pressure the superconducting phase starts emerging and magnetism is gradually suppressed, see Figure 2a.

The $CeTX_3$ compounds exhibit various magnetic ground states from antiferromagnetic (AFM) heavy fermion (HF) states to intermediate valence (IV), see Table 1 for $CeTX_3$ with T from the Group 9 (Co, Rh, Ir). For the develop-

[1] It is worth mentioning that noncentrosymmetric superconductors have been also been reported among the related $(Ca, La)TSi_3$ compounds [16, 17, 18].

ment of T_N with unit-cell volume V a simple curve has been proposed supporting the Doniach model in which the on-site Kondo effect dominates over the inter-site RKKY interaction with decreasing V [19]. We have studied this development within the course of my bachelor thesis in Ref. [20], results are plotted in Figure 2b.

	Mag. GS	γ [mJ/molK^2]	T_N [K]	θ_p [K]	μ_{eff} [μ_B/Ce]	**Ref.**
$CeCoSi_3$	PM(IV)	37	-	-840	2.80	[21]
$CeRhSi_3$	AFM(HF)	120	1.8	-128	2.65	[22]
$CeIrSi_3$	AFM(HF)	125	5.0	-142	2.62	[22]
$CeCoGe_3$	AFM	32	21/12/8	-29*	2.16*	[10]
$CeRhGe_3$	AFM	40	14.9/8.2/0.55	-28	2.53	[22, 23]
$CeIrGe_3$	AFM	80	8.7/4.8/0.7	-21	2.39	[22, 23]

Table 1: Magnetic ground state (GS), Sommerfeld coefficient γ, ordering temperature T_N, Curie-Weiss temperature θ_p, effective magnetic moment μ_{eff} of $BaNiSn_3$ type $CeTX_3$ compounds. The values denoted by * were measured on single crystals with $H||[001]$.

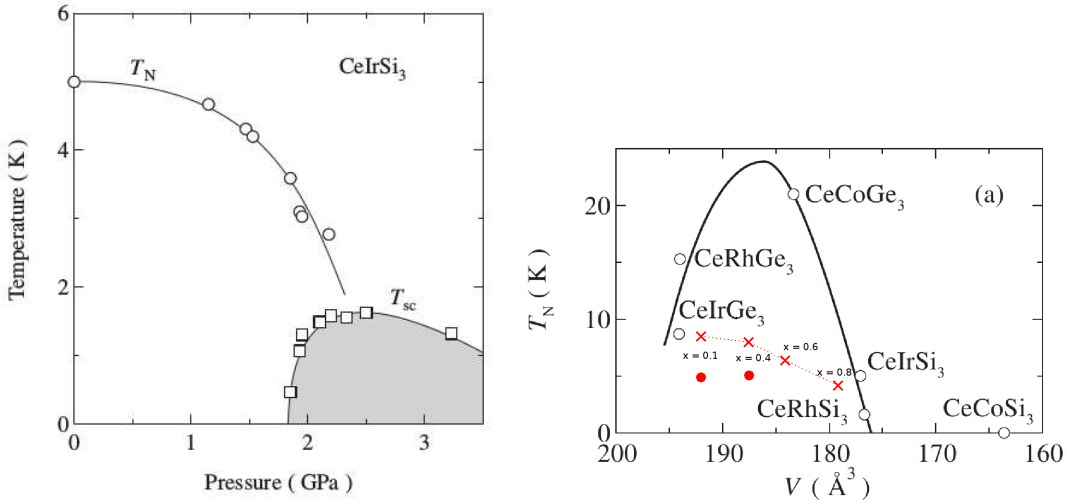

(a) (b)

Figure 2: (a) Temperature-pressure phase diagram of $CeIrSi_3$, T_N denotes the Néel temperature and T_{SC} the superconducting transition temperature, reprinted from Ref. [13]. (b) Unit cell volume dependence of the Néel temperature in $CeTX_3$ (T: Co, Rh, Ir), reprinted from Ref. [23], with the results from measurements of $CeIr(Si_xGe_{1-x})_3$ from Ref. [20] plotted as diagonal stars.

'Devil's staircase' Systems

A typical example of a 'devil's staircase' system is the CeSb. It exhibits the characteristic feature of the system – the step-like behaviour of magnetization in

increasing magnetic field caused by successive magnetic phase transitions (similarly to the magnetization of $CeCoGe_3$ in Figure 3). The CeSb crystallizes in the rock salt structure and all the phases consist of square-wave structures with propagation vector $\boldsymbol{k} = (0, 0, k)$ and the moments along the $\boldsymbol{k}$ vector. The structures of the various phases can be described by a periodic stacking of zero magnetized and ferromagnetic planes with parallel or antiparallel magnetization, e.g. structures with $k = 4/7$ $(++--++-)$, $k = 2/3$ $(++-)$ and $k = 0$ are successively observed at low temperatures with increasing field. Many other phases are observed depending on the conditions (temperature or applied magnetic field) of the experiment, the complete magnetic phase diagram is displayed in Figure 4 [24].

However, a compound more relevant to the studied $CeCo_{0.715}Si_{2.285}$ is the $CeCoGe_3$. It is a member of the $CeTX_3$ group and besides the above–mentioned properties its magnetization for $H||[001]$ also exhibits a feature characteristic for the 'devil's staircase' systems – three step-like metamagnetic transitions as shown in Figure 3. It is an antiferromagnet with a Néel temperature of $T_{N1} = 21$K and two other successive transitions at $T_{N2} = 12$K and $T_{N3} = 8$K. All three transitions are visible in the resistivity data for $J||[001]$ as well as in the magnetization data. The magnetic susceptibility follows the Curie-Weiss law at temperatures above 150K with effective magnetic moment and paramagnetic Curie-Weiss temperature of $\mu^{||a}_{\mathrm{eff,CeCoGe_3}} = 2.23\mu_B$/Ce and $\theta^{||a}_{\mathrm{p,CeCoGe_3}} = -71$K for $H||[100]$ and $\mu^{||c}_{\mathrm{eff,CeCoGe_3}} = 2.16\mu_B$/Ce and $\theta^{||c}_{\mathrm{p,CeCoGe_3}} = -29$K for $H||[001]$, respectively. The magnetic ordering is manifested in specific heat data as a sharp, almost λ-like anomaly at $T_{N1} = 21$K, the Sommerfeld coefficient below this ordering temperature equals $\gamma_{\mathrm{CeCoGe_3}} = 32\mathrm{mJ/molK^2}$ and the magnetic entropy gain reaches $\Delta S_{\mathrm{CeCoGe_3}} = 0.68\ln 2$ at T_{N1} [10]. Its magnetic structure is displayed in Figure 4.2.

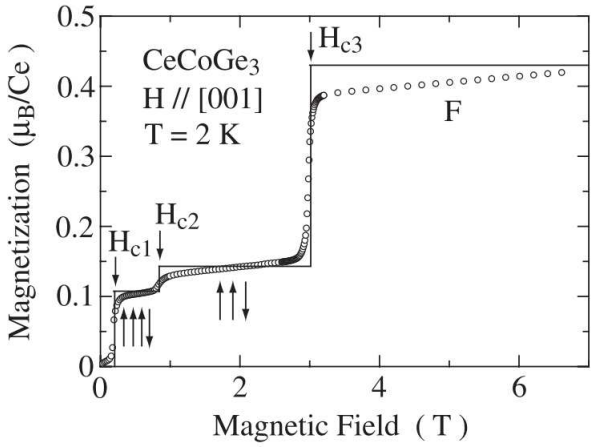

Figure 3: Magnetic field dependence of magnetization of $CeCoGe_3$ [10].

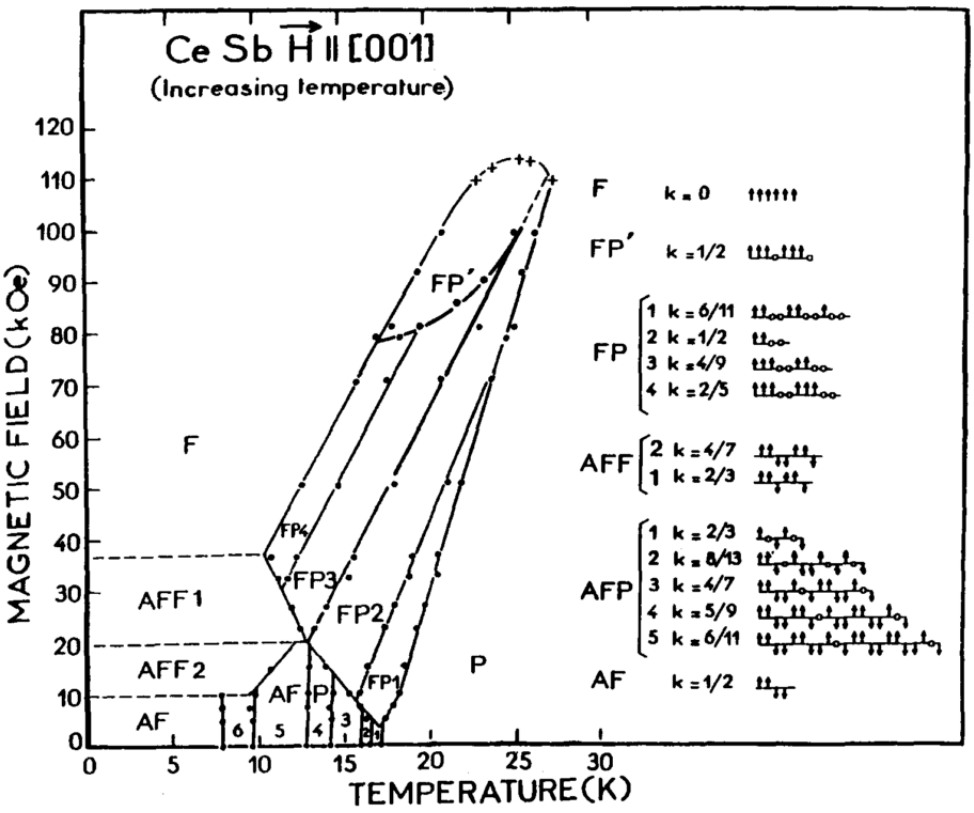

Figure 4: Magnetic phase diagram of CeSb, reprinted from Ref. [9].

1. Theory

1.1 Magnetism

Magnetic moment can be defined in the following way: Let us consider a current I flowing in a loop which encloses an area S and let the vector $\boldsymbol{S}$ point in the direction normal to the plane. Then the magnetic moment created equals $\boldsymbol{m} = I\boldsymbol{S}$, its units are Am^2. Using basic theory of electromagnetism we see that such definition of magnetic moment also defines the forces which it experiences in an external magnetic field and we can thus also define magnetic moment via the torque it experiences in such fields. We will usually express magnetic moment in units of Bohr magneton $\mu_\mathrm{B} = \mathrm{e}\hbar/2\mathrm{m_e} = 9.27 \cdot 10^{-24}\mathrm{JT}^{-1}$ [25].

A magnetic moment of a free atom has three principal sources: the spin with which the electrons are endowed; their orbital angular momentum; and the change in the orbital moment induced by an applied magnetic field [26]. Lets assume a solid to constitute of a large number of atoms each having an individual magnetic moment and a magnetization of such solid then to be the averaged vector sum of those moments normalized to, for example, a unit volume or a formula unit.

Depending on the reaction of the studied material to an external magnetic field we can, in the simplest case, classify magnetism as

diamagnetism – magnetization of the material is negative in non-zero fields but zero in zero magnetic field,

paramagnetism – magnetization of the material is positive in non-zero fields but zero in zero magnetic field,

ferromagnetism – magnetization of the material is non-zero in both non-zero and zero magnetic fields.

The last mentioned ferromagnetism occurs in the so-called magnetically ordered solids. In such solids below a critical temperature the magnetic moments are subject to certain magnetic interactions causing the emergence of a long range magnetic order which in turn results in the non-zero magnetization in zero magnetic fields – the so called spontaneous magnetization. Apart from the mentioned ferromagnets, there is a number of various magnetically ordered materials with both non-zero and zero spontaneous magnetization, e.g. antiferromagnets or ferrimagnets.

A ferromagnetically ordered solid exhibits a spontaneous magnetization below the critical *Curie temperature* T_C. Increasing the temperature and therefore increasing the entropy of the system eventually causes a breaking of the magnetic order and a transition to the disordered paramagnetic state. The usual transition from ferromagnetic to paramagnetic state is of second order [26], see Equation 1.35.

Using the *mean-field approximation*, we assume that each magnetic atom experiences apart from the applied external magnetic field another field B_E, called the exchange field, which is proportional to the magnetization $B_\mathrm{E} = \lambda M$. If we assume that a ferromagnet is a paramagnet with the additional magnetization

caused by the exchange field we can derive an expression for a magnetic susceptibility χ of a ferromagnet in the paramagnetic region above the Curie point – the Curie-Weiss law [26, Equation 12.4]

$$\chi = \frac{C}{T - T_{\mathrm{C}}}. \tag{1.1}$$

Another ordered magnetic state relevant to this study is the antiferromagnetic state in which the vector sum of the individual magnetic moments sums up to zero. An antiferromagnet thus does not exhibit a spontaneous magnetization even though the magnetic moments display a long-range order. A simple illustration of such mechanism is a case when all magnetic moments are of the same absolute value but neighbouring moments point in quite the opposite direction – such system is obviously ordered but the sum of all the moments over the whole macroscopic sample of such solid is zero. The critical temperature above which this ordering is no longer present is called the *Néel temperature* T_{N}.

Above the Néel temperature T_{N} an antiferromagnet obeys the Curie-Weiss law in the form [26, Equation 12.20]

$$\chi = \frac{C}{T - \theta_{\mathrm{p}}} \tag{1.2}$$

where θ_{p} denotes the paramagnetic Curie-Weiss temperature – it has the same meaning as the Curie temperature for ferromagnet, it is only of negative value. From the Curie-Weiss constant C one can calculate the effective magnetic moment μ_{eff} using the relation [26, Equation 11.22]

$$C = \frac{N \mu_{\mathrm{B}}^2 \mu_{\mathrm{eff}}^2}{3 k_{\mathrm{B}}} \tag{1.3}$$

where k_{B} is the Boltzmann constant. If $[C]$ = emu/mol the relation for the effective magnetic moment is

$$\mu_{\mathrm{eff}} = \sqrt{\frac{3 C k_{\mathrm{B}}}{N_{\mathrm{A}} \mu_{\mathrm{B}}^2}} \tag{1.4}$$

where N_{A} is the number of constituent particles (atoms, molecules...) contained in one mole.

1.1.1 Electronic Structure

Until now we have described bulk properties of magnetically ordered materials and have talked about the underlying long range order of the magnetic moments. Now, we would like to briefly describe the formation of magnetic moment and magnetic order on a microscopic scale via description of electronic states in the material.

Free Ion

A free ion consists of a nucleus and electrons surrounding it and to successfully describe the electrons' behaviour one has to use the quantum mechanics. Each

electron is described by a wave function which is specified via 4 quantum numbers: principal quantum number n, orbital quantum number l, magnetic quantum number m and spin quantum number s. The value of principal quantum number ranges from 1, $n = 1, 2, 3...$, the orbital one has values $l = 0, 1, 2, \cdots, n-1$, the magnetic $m = 0, \pm 1, \pm 2, \cdots, \pm l$ and the spin one $s = \pm 1/2$. The orbital quantum number l is used to label the subshell of the electron as 's' for $l = 0$, 'p' for $l = 1$, 'd' for $l = 2$, 'f' for $l = 3$, etc. It characterises the internal angular structure of the electron state and depending on its 'orientation' with respect to the z-axis the z-component of angular momentum of the electron can be $m = 0, \pm 1, \pm 2, \cdots, \pm l$ [27].

Let us now consider a free ion with an incompletely filled f shell. The orbital quantum number $l = 3$, there are $2l + 1 = 7$ possible values of magnetic quantum number m and for each of these states two values of spin quantum number s are possible. We therefore can have up to $2(2l + 1) = 14$ electrons (different electronic states) in such a shell. In our case, however, the shell is incompletely filled and the question therefore is which ones of these 14 states are occupied. This is specified by the *Hund rules* that describe the properties of the ground state as,

- firstly, that for a given configuration the term with the maximum spin S (called maximum multiplicity) possesses the lowest energy,
- secondly, for a given configuration and multiplicity the term with the largest value of the angular momentum L possesses the lowest energy and
- thirdly, for the given configuration, multiplicity and angular momentum the value of the total angular momentum J is a minimum ($J = |L - S|$) if the configuration represents a less than half-filled shell but is a maximum ($J = |L + S|$) if the shell is more than half-filled [28].

The rules therefore give a sequence of occupation of the electronic states.

For example, in the case of Ce^{3+} ion we only have a single electron in the f shell and by applying the Hund rules we obtain $S = 1/2, L = 3, J = 5/2$. We have now determined how the ground state in our ion looks like and which electron states are occupied and which are not. From the values of spin, orbital and total angular momentum which characterize this ground state we are able to derive the size of the magnetic moment μ and effective magnetic moment μ_{eff} of the free ion as [26, Equation 11.11], [28, Equation 4.1]

$$\mu = -g\mu_{\text{B}}J, \qquad \mu_{\text{eff}} = g\mu_{\text{B}}\sqrt{J(J+1)} \tag{1.5}$$

where g is the Landé g-factor given by [26, Equation 11.13]

$$g = 1 + \frac{J(J+1) + S(S+1) - L(L+1)}{2J(J+1)}. \tag{1.6}$$

Taking Ce^{3+} ion again as an example, we get $g = 6/7$, $\mu \simeq 2.14\mu_{\text{B}}$ and $\mu_{\text{eff}} \simeq 2.54\mu_{\text{B}}$.

Ion in a Lattice

So far we have discussed the case of a free ion. The next logical step is to ask what happens when this ion is placed in a crystal lattice. There are basically two limit cases which can model behaviour of ions of different elements.

In the *localized limit* the wave functions describing the electronic structure together with the consequently arising magnetic moments keep their free-ion like nature and the effects of the surrounding ions (atoms) and electrons are introduced separately. This approach is applicable in the case of the $4f$ electron system – lanthanides. The above–described calculation of magnetic moment using Hund rules is in a good agreement with experimental values, see Table 11.1 in Ref. [26], for the whole series from Ce^{3+} ion to Yb^{3+} ion with the exceptions of Sm^{3+} and Eu^{3+} whose values differ. The introduction of the effects of the surrounding ions and electrons can be done via the so-called *exchange interactions* (see below) or, for example, the so-called *crystalline electric field* (CEF) which is in principle a Coulomb interaction of the cation (Ce^{3+} for example) with the surrounding charged particles (other ions Ce^{3+} and electrons of the completely filled s and d shells). It is worth noting that the CEF reflects the structure of the material and may be anisotropic.

The second limit is the so-called *itinerant limit* – from Latin *itineris* which is genitive singular of *iter*, a journey, march or a road. The magnetism in this limit stems from the delocalized ('itinerant', 'travelling') nature of electrons. Even though presently not all cases are fully understood it seems clear that the $T = 0$ properties of a majority of metallic magnets, excluding those involving rare earths, can be explained in the itinerant electron picture [28]. The magnetic properties of numerous elements (e.g. Fe) can be described using the band theory, originally proposed by Stoner [29, 30]. In the simplest case, the mechanism can be described as follows: the periodic potential breaks up the atom states and redistributes the valence electrons in Bloch states. The electrons moving in the periodic potential are thus characterised by quantum number n, that serves as a band index, wave vector $\boldsymbol{k}$ and a spin projection which we can choose either up or down. One then introduces a difference in the number of up and down electrons and probes the stability of such state in terms of energy minimization. The criterion that arises is the so-called *Stoner condition* which states that the non-magnetic state is unstable when [28, Equation 4.35]

$$\mathcal{N}_0 I > 1, \qquad \mathcal{N}_0 = \frac{3}{2}\frac{1}{\epsilon_{\mathrm{F}}} \tag{1.7}$$

where $\mathcal{N}_0$ is the spin-added density of states at the Fermi energy ϵ_{F} and I is the molecular field constant.

Exchange Interactions

As mentioned, the exchange interactions introduce the effects of the surrounding ions and electrons on the magnetic moments on the studied ion (atom).

Firstly a *direct exchange interaction* should be considered. It occurs in the case when the wave functions of electrons responsible for magnetic moments of the neighbouring atoms overlap. It is called direct since the electrons interact directly with each other without any other particle intermediating the interaction. The interaction is written as

$$\mathcal{H}_{\mathrm{ex}}^{ij} = -2J_{ij} \cdot S_i S_j \tag{1.8}$$

with J_{ij} being the so-called *exchange integral* and $S_{i,j}$ the magnetic spin vectors. The exchange interaction originates from a quantum exchange term of the

Coulomb interaction between d electrons of the neighbouring ions so that it has the coupling strength of the Coulomb interaction, as discussed by Heisenberg in 1928.

By contrast, the *indirect exchange interaction* (or *superexchange*) arises between two magnetic ions via some other particle which mediates the interaction. This can be anions situated between the ions [31] or conduction electrons. The latter is the so-called RKKY interaction (named after the four persons responsible for its development – M. A. Ruderman, C. Kittel, T. Kasuya and K. Yosida). Being originally developed for description of indirect interaction of nuclear magnetic moments in a metal [32] the RKKY interaction has later been applied to the interaction of unfilled inner shell electrons [33, 34]. The conduction electron interacts with the localized unfilled inner shell electrons of one ion and the interaction is reflected in its wave function. This is in turn seen by the neighbouring ion and the mechanism thus establishes an indirect spin-dependent coupling between the two ions. This mechanism is especially important in a description of magnetic moments and long range magnetic order of $4f$ ions (as Ce^{3+} for example).

Another noteworthy interaction is the *Kondo interaction* (or *s-d* exchange interaction) and the consequent Kondo effect firstly described by Jun Kondo in Ref. [35]. The conduction electrons of a dilute magnetic alloy scatter on localized electrons of the magnetic impurity and a then arising Kondo effect is observed as a minimum in the temperature dependence of electrical resistivity. In order to describe this behaviour a term $\rho_{\mathrm{spin}} \sim \log(T)$ is introduced into the formula describing temperature dependence of resistivity as a sum of terms (each arising from a different scattering source) – the so-called Matthiessen's rule [36, Equation 1]. The model is derived for the case when the exchange interaction J between the conduction and localized electrons is negative (favourable for antiparallel spins) [35].

1.2 Diffraction on Crystal and Magnetic Structure

1.2.1 Crystal Structure

An ideal crystal is a long-range ordered material made of atoms which are ordered on a lattice defined by three vectors $\mathbf{a}, \mathbf{b}, \mathbf{c}$ such that the arrangement looks the same from each point [26, Equation 1.1]

$$\boldsymbol{R_n} = n_1\mathbf{a} + n_2\mathbf{b} + n_3\mathbf{c}, \qquad n_{1,2,3} \in \mathcal{Z} \tag{1.9}$$

where $\mathcal{Z}$ is the set of integers. The set of such points $\boldsymbol{R_n}$ defines a lattice. A parallelepiped formed by the three vectors $\mathbf{a}, \mathbf{b}, \mathbf{c}$ is called a unit cell. For this lattice to describe a crystal we must add a certain appropriate basis of atoms to each lattice point. If all points from which the arrangement of atoms looks the same satisfy Equation 1.9 we call the lattice primitive and the parallelepiped formed by the three vectors $\mathbf{a}, \mathbf{b}, \mathbf{c}$ is then called primitive unit cell. However, a much more convenient is the use of the so-called elementary cell which is the smallest possible parallelepiped which has a full point symmetry of the lattice. An elementary unit cell need not equal to the primitive unit cell.

When trying to describe a diffraction of a wave on a periodic crystal lattice a concept of *reciprocal lattice* is very useful. Reciprocal lattice basis vectors $\mathbf{a}^*, \mathbf{b}^*, \mathbf{c}^*$ can be defined as [26, Equation 2.13]

$$\mathbf{a}^* = 2\pi\frac{\mathbf{b}\times\mathbf{c}}{\mathbf{a}\cdot\mathbf{b}\times\mathbf{c}}, \mathbf{b}^* = 2\pi\frac{\mathbf{c}\times\mathbf{a}}{\mathbf{a}\cdot\mathbf{b}\times\mathbf{c}}, \mathbf{c}^* = 2\pi\frac{\mathbf{a}\times\mathbf{b}}{\mathbf{a}\cdot\mathbf{b}\times\mathbf{c}} \tag{1.10}$$

and reciprocal lattice vectors then take the form of

$$\boldsymbol{G}_{hkl} = h\mathbf{a}^* + k\mathbf{b}^* + l\mathbf{c}^*, \qquad h,k,l \in \mathcal{Z}. \tag{1.11}$$

The importance of such (artificially) defined lattice is that the measured diffraction pattern is a map of the reciprocal lattice as opposed to direct microscopic optic experiments which map the direct crystal lattice.

If we consider a function $f(\mathbf{r})$ which is periodic in the 3D primitive lattice, like the electron density function $\rho(\mathbf{r})$, we can express it as a Fourier series in a reciprocal lattice like [26, Equation 2.9]

$$f(\mathbf{r}) = \sum_{\boldsymbol{G}} f_{\boldsymbol{G}} \mathrm{e}^{\mathrm{i}\boldsymbol{G}\cdot\mathbf{r}}. \tag{1.12}$$

Diffraction on Crystal Structure

Let us now consider an elastic scattering of a monochromatic radiation. Let $\boldsymbol{K}_0$ be the wave vector of the incident and $\boldsymbol{K}$ of the diffracted wave and $\boldsymbol{Q} \stackrel{\text{def}}{=} \boldsymbol{K} - \boldsymbol{K}_0$ the so-called scattering vector. We then can derive the condition for a diffraction of the radiation on a (hkl) plane as [37, equation 3.15]

$$\boldsymbol{K} - \boldsymbol{K}_0 = \boldsymbol{Q} = \boldsymbol{G}_{hkl} \tag{1.13}$$

or as the so-called Laue equation. The condition is equivalently expressed in the so-called *Bragg law* [26, equation 2.1]

$$2d\,\sin(\theta) = n\lambda, \qquad n \in \mathcal{N} \tag{1.14}$$

where d is the spacing between parallel lattice planes (hkl), θ the angle of incidence, λ the wavelength of the incident wave and $\mathcal{N}$ the set of natural numbers.

We have now stated diffraction conditions for a diffraction of a radiation on a general set of equidistant planes, i.e. in the simplest model of a crystal possible. If we want to describe diffraction on a more complex model of a crystal things get a bit more complicated and complete explanation exceeds the ambitions of this section of this study. We will only briefly describe formulas for calculating intensity of radiation diffracted from a small perfect crystal which is (as a whole) coherently irradiated by a beam of monochromatic X-Ray radiation. We will describe this situation within the kinematical approximation in which multiple scattering is neglected, i.e. each photon is scattered only once (this condition is valid in case of a structurally imperfect (randomly disturbed) crystals). We will also limit ourselves only to elastic Thomson scattering during which the energy stays conserved and therefore also the wavelength of the incident wave remains unchanged. Let the crystal be a parallelepiped whose sides are of length

M_1a, M_2b, M_3c ($M_{1,2,3} \in \mathcal{N}$) and which therefore contains $M = M_1M_2M_3$ elementary unit cells. If the diffraction condition 1.13 is fulfilled ($\boldsymbol{Q} = \boldsymbol{G}_{hkl}$) then the intensity of the diffracted radiation can be expressed as [37, Equation 4.50]

$$I = I_e F_{hkl}^2 M^2. \tag{1.15}$$

It depends on I_e, the intensity of coherently scattered unpolarized radiation on a classical free electron (see [37, Equation 4.12]), and F_{hkl} which is the so-called structure factor and equals to the Fourier transform of the electron density of atoms belonging to the same elementary unit cell. It can be calculated using [37, Equation 4.33]

$$F_{hkl} = \sum_{n=1}^{N} f_n(k) \mathrm{e}^{[2\pi \mathrm{i}(hx_n + ky_n + lz_n)]} \tag{1.16}$$

where the summation is over all N atoms belonging to the same elementary unit cell, x_n, y_n, z_n are their fractional coordinates and f_n their atomic scattering factors which for spherically symmetric atoms equal [37, Equation 4.21]

$$f_n(k) = \int_0^\infty 4\pi r^2 \rho(r) \frac{\sin kr}{kr} \mathrm{d}r. \tag{1.17}$$

It should also be stated that the above is valid only if the whole scattering object is much smaller than $\sqrt{\lambda R}$ where R is the observation distance, i.e. the so-called Fraunhofer (or far-field) approximation [38, Equation 4.27].

1.2.2 Magnetic Structure

In order to fully describe the structure of a crystal that contains atoms with non-zero magnetic moments one has to determine how the magnetic moments are distributed in the crystal lattice – where do they sit, in which direction they point and how large they are. Since magnetic moment (its size and direction) of equivalent atoms in the lattice can differ across different elementary cells the magnetic structure must be described by a magnetic unit cell, which does not necessarily have the same size as the elementary (nuclear) cell. To make the description as simple and compact as possible a concept of a so-called propagation vector $\boldsymbol{k}$ is very useful. Let us have a magnetic moment $\boldsymbol{m}_{nj}$ at position

$$\boldsymbol{R_{n}}_j = \boldsymbol{R_n} + \boldsymbol{r}_j \tag{1.18}$$

where

$$\boldsymbol{r}_j = x\mathbf{a} + y\mathbf{b} + z\mathbf{c}, \qquad 0 \leq x, y, z \leq 1, \quad x, y, z \in \mathcal{R} \tag{1.19}$$

and $\mathcal{R}$ denotes the set of real numbers. The spatial distribution of magnetic moment $\boldsymbol{m}_{nj}$ can be Fourier expanded (due to its spatial periodicity) as [39, equation (10)]

$$\boldsymbol{m}_{nj} = \sum_{\boldsymbol{k}} \Psi_j^{\boldsymbol{k}} \mathrm{e}^{(-2\pi \mathrm{i} \boldsymbol{k} \cdot \boldsymbol{R_n})} \tag{1.20}$$

where $\Psi_j^{\boldsymbol{k}}$ is a basis vector which (if real) corresponds to the projection of the moment along crystallographic axes in the 0^{th} cell. Using this concept we only need the information about the nuclear elementary cell, propagation vector(s) $\boldsymbol{k}$ and the basis vector(s) $\Psi_j^{\boldsymbol{k}}$ to fully describe the magnetic structure.

Diffraction on Magnetic Structure

Magnetic structure can be studied via diffraction of a beam of neutrons on the studied crystal. The key property of neutrons allowing such experiments is their intrinsic magnetic dipole moment $\mu_\mathrm{n} = -1.913\mu_\mathrm{N}$ ($\mu_\mathrm{N} = 5.051 \cdot 10^{-27}\mathrm{JT}^{-1}$ is the nuclear magneton) [25]. Due to its non-zero value neutrons interact not only with atomic nuclei via short range forces but also with, for example, spin and orbital angular momentum of unpaired electrons via a magnetic dipole interaction.

In the case of elastic scattering the intensities of nuclear and magnetic diffractions are additive and the diffracted intensity is proportional to the square of the so-called magnetic interaction vector $\boldsymbol{F}_\perp(\boldsymbol{Q})$ (the component of the magnetic structure factor perpendicular to the scattering vector $\boldsymbol{Q}$) [40, Equation 3]

$$I(\boldsymbol{Q}) = K(\boldsymbol{Q})\boldsymbol{F}_\perp(\boldsymbol{Q}) \cdot \boldsymbol{F}^*_\perp(\boldsymbol{Q}) \tag{1.21}$$

where $K(\boldsymbol{Q})$ includes geometrical terms. For the integrated intensity of a magnetic diffraction (hkl) we can then write (except for a constant factor)

$$I(\boldsymbol{Q}) = K(\boldsymbol{Q})\left\{|\boldsymbol{F}_\mathrm{m}(\boldsymbol{Q})|^2 - \left|\frac{\boldsymbol{Q}\cdot\boldsymbol{F}_\mathrm{m}(\boldsymbol{Q})}{Q}\right|^2\right\} \tag{1.22}$$

where $\boldsymbol{F}_\mathrm{m}$ is the magnetic structure factor of the unit cell which can be calculated using [40, Equation 8]

$$\boldsymbol{F}_\mathrm{m}(\boldsymbol{G}_{hkl} + \boldsymbol{k}) = p\sum_s f_s(\boldsymbol{Q})\sum_j \Psi^{\boldsymbol{k}}_j(s)\boldsymbol{W}_{sj}(\boldsymbol{Q})\mathrm{e}^{\{2\pi\mathrm{i}(\boldsymbol{G}_{hkl}+\boldsymbol{k})\boldsymbol{r}_j(s)\}}. \tag{1.23}$$

The s labels the Wyckoff position of multiplicity r, $j = (1, 2, \ldots, r)$ labels equivalent Bravais sublattices of such position, p is a constant, $f_s(\boldsymbol{Q})$ the form factor of the chemical species and $\boldsymbol{W}_{sj}$ the Debye-Waller factor. From the expression 1.23 we can conclude that only the Fourier components $\Psi^{\boldsymbol{k}}_j$ of the magnetic structure are accessible from neutron diffraction experiment. For experimental data analysis (among other possible approaches) one thus performs analysis of the irreducible representations of the propagation vector group and their associated basis functions. A certain knowledge of group theory is thus very useful and we will briefly describe certain relevant concepts of it in the next section.

Group Theory

A group $\mathcal{G}$ is a set of elements g, $g \in \mathcal{G}$, together with an operation that combines two elements g_1 and g_2 to form another element g_1g_2. The set and operation must satisfy four requirements

- closure: $g_ig_j = g_k$,
- associativity: $g_i(g_jg_k) = (g_ig_j)g_k = g_ig_jg_k$,
- existence of an identity element e: $eg = ge = g$,
- existence of an inverse element g^{-1}: $gg^{-1} = g^{-1}g = e$.

Let $\mathcal{G}_0$ be the space group of symmetry elements $g \stackrel{\text{def}}{=} \{A, \boldsymbol{t}\}$ of the studied structure where A is the rotation and $\mathbf{t}$ translation part of the element. We then define the 'little group' $\mathcal{G}_{\boldsymbol{k}}$ as the group consisting of symmetry elements of $\mathcal{G}_0$ that leave $\boldsymbol{k}$ invariant, i.e. if g_1 is an element of $\mathcal{G}_{\boldsymbol{k}}$ and

$$\boldsymbol{k_1} = g_1 \boldsymbol{k} \tag{1.24}$$

then $\boldsymbol{k_1}$ and $\boldsymbol{k}$ are equal.

Let $\mathcal{V}$ be a vector space and let for all $g \in \mathcal{G}$ exist a regular linear operator $\mathcal{D}(g) : \mathcal{V} \to \mathcal{V}$ and let

(i) $\mathcal{D}(e) = 1$ and

(ii) $g_i g_j = g_k$ imply $\mathcal{D}(g_i)\mathcal{D}(g_j) = \mathcal{D}(g_k)$.

We then call $\mathcal{D}$ a representation of a group $\mathcal{G}$ on a vector space $\mathcal{V}$. A representation of a point group of a molecule symmetry, for example, would look as follows. Let the atoms of the molecule sit at $\boldsymbol{R}$ and let a vector space $\mathcal{V}$ have orthonormal basis made of vectors $|\boldsymbol{R}\rangle$. The point group of the molecule symmetry $\mathcal{G}$ then consists of rotation, mirror symmetry or their combination. An $A \in \mathcal{G}$ transforms vectors of atoms of the molecule again to vectors of atoms of the molecule which then leads to the definition of a representation $\mathcal{D}(A)$ by its effect on the basis vectors as

$$\mathcal{D}(A)|\boldsymbol{R}\rangle = |A\boldsymbol{R}\rangle \tag{1.25}$$

where there sits for every atom $\boldsymbol{R}$ and every $A \in \mathcal{G}$ an atom at $A\boldsymbol{R}$.

Reducibility of a representation $\mathcal{D}$ of a group $\mathcal{G}$ on a vector space $\mathcal{V}$ means that one can decompose the vector space $\mathcal{V}$ into subspaces $\mathcal{V}^{(\nu)}$, $\nu = 1, 2, ..., M$,

$$\mathcal{V} = \mathcal{V}^{(1)} \oplus \mathcal{V}^{(2)} \oplus ... \oplus \mathcal{V}^{(M)} \tag{1.26}$$

such that for all ν and $g \in \mathcal{G}$ the representation is $\mathcal{D}(g) : \mathcal{V}^{(\nu)} \to \mathcal{V}^{(\nu)}$. We can write that

$$\mathcal{D} = \mathcal{D}^{(1)} \oplus \mathcal{D}^{(2)} \oplus ... \oplus \mathcal{D}^{(M)}. \tag{1.27}$$

If there exists no such decomposition of $\mathcal{V}$ then the representation $\mathcal{D}$ is irreducible.

The above–mentioned experimental data analysis is then based on the following approach. Firstly, the irreducible representations $\mathcal{D}^{(\nu)}$ of the little group $\mathcal{G}_{\boldsymbol{k}}$ are calculated, followed by the basis functions $V^{\boldsymbol{k},\nu}_{a,m,j}$. The basis functions correspond to magnetic moments of atoms and the basis vector $\Psi^{\boldsymbol{k}}_j$ can be written as their linear combination

$$\Psi^{\boldsymbol{k}}_j = \sum_{a,m} C_{a,m} V^{\boldsymbol{k},\nu}_{a,m,j} \qquad a = 1, \ldots, \dim(\mathcal{D}^{(\nu)}) \tag{1.28}$$

where $C_{a,m}$ are coefficients and m varies from 1 to the number of times the irreducible representation $\mathcal{D}^{(\nu)}$ is contained in the global magnetic irreducible representation.

1.3 Thermodynamic Properties

Phase Transitions

Heat capacity is an important thermodynamic quantity defined as follows. If a homogeneous system absorbs a small amount of heat $\mathrm{d}Q$ causing its temperature to rise by $\mathrm{d}T$ then its heat capacity at constant pressure C_p is

$$C_\mathrm{p} = \left(\frac{\mathrm{d}Q}{\mathrm{d}T}\right)_\mathrm{p}. \tag{1.29}$$

Specific heat c_p is then a heat capacity per unit mass or per mole. Another important quantity is entropy S. The change in entropy can be calculated using the specific heat (under the assumption that no work is being carried out) as

$$\Delta S = \int \frac{C(T)}{T}\,\mathrm{d}T. \tag{1.30}$$

The quantity

$$l = T\Delta s \tag{1.31}$$

is then called the specific latent heat of a transition where Δs denotes a change in entropy per unit mass. When considering a phase transition from solid to liquid phase, for example, the latent heat of the transition is the quantity of heat required to melt one unit mass of solid.

Gibbs free energy is a thermodynamic potential defined as

$$G(p,T) = U + pV - TS \tag{1.32}$$

with its total differential being

$$\mathrm{d}G = V\mathrm{d}p - S\mathrm{d}T. \tag{1.33}$$

It can be shown that isobaric specific heat and entropy equal

$$c_\mathrm{p} = -T\left(\frac{\partial^2 G}{\partial T^2}\right)_\mathrm{p}, \qquad S = -\left(\frac{\partial G}{\partial T}\right)_\mathrm{p}. \tag{1.34}$$

Ehrenfest defines the order of a phase transition using the derivatives of the Gibbs potential per unit mass g_i of the two phases. The transition is of nth order if at the transition point [41]

$$\frac{\partial^n g_1}{\partial T^n} \neq \frac{\partial^n g_2}{\partial T^n} \qquad \text{and} \qquad \frac{\partial^n g_1}{\partial P^n} \neq \frac{\partial^n g_2}{\partial P^n} \tag{1.35}$$

whereas all lower derivatives are equal.

Since entropy is related to the first derivative of Gibbs potential g and the specific heat is related to the 2nd derivative of g, see Equation 1.34, during the first order phase transition we observe a discontinuity in entropy and according to Equation 1.31 a latent heat is absorbed/released. During a second order phase transition on the other hand, the second derivatives of Gibbs potential are not continuous and thus neither is the specific heat. A well-known example of a second-order transition is the transition to a superconducting state.

Specific Heat

Specific heat of the studied system – a crystal – as well as its entropy can be described as a sum of contributions of its individual components, e.g.

$$c_{\mathrm{p}}(T) = c_{\mathrm{el}}(T) + c_{\mathrm{ph}}(T) + c_{\mathrm{mag}}(T) + c_{\mathrm{etc}}(T) \tag{1.36}$$

where $c_{\mathrm{el}}(T)$ denotes the contribution from conduction electrons, $c_{\mathrm{ph}}(T)$ the contribution from lattice vibrations (*phonons*), $c_{\mathrm{mag}}(T)$ the magnetic contribution and $c_{\mathrm{etc}}(T)$ other contributions.

The specific heat contribution from conduction electron gas depends linearly on temperature [26, Equation 6.37]

$$c_{\mathrm{el}}(T) = \gamma T. \tag{1.37}$$

To interpret the experimental values of the coefficient γ, the so-called *Sommerfeld coefficient*, one can compare it with the values obtained from the electronic heat capacity of a free electron and express their ratio as a ratio of a thermal effective mass m^* to the free electron mass m_e [26, Equation 6.38]

$$\frac{m^*}{m_{\mathrm{e}}} = \frac{\gamma_{observed}}{\gamma_{free}}. \tag{1.38}$$

The ratio differs from unity due to numerous interactions that the conduction electrons are subject to, e.g. interaction with phonons in which the moving electron tends to distort the lattice in its vicinity and drag the surrounding ions along resulting in an increase in the electron's effective mass. Compounds with effective masses of enormous values (up to $1000m_{\mathrm{e}}$) are called heavy fermions.

Phonon is a quantum unit of a crystal vibration. If the angular frequency of a vibration is ω then the phonon is a quasiparticle with energy $\hbar\omega$ ($\hbar$ is the Planck constant divided by 2π). The phonon contribution to specific heat can be approximated using numerous models. The so-called Debye model describes the phonons as a set of harmonic oscillators of frequencies up to a cutoff frequency ω_{D}. From its value one can calculate the so-called *Debye temperature* as [26, Equation 5.27]

$$\theta_{\mathrm{D}} = \hbar\omega_{\mathrm{D}}/k_{\mathrm{B}}. \tag{1.39}$$

The phonon contribution to specific heat can then be expressed as [26, Equation 5.30]

$$c_{\mathrm{ph}}(T) = 9n\mathrm{R}\left(\frac{1}{x_{\mathrm{D}}}\right)^3 \int_0^{x_{\mathrm{D}}} \frac{x^4 e^x}{(e^x-1)^2}\mathrm{d}x, \qquad x_{\mathrm{D}} = \frac{\theta_{\mathrm{D}}}{T} \tag{1.40}$$

where n is the number of atoms per formula unit and R is the gas constant. This approach is able to describe experimental data quite well, however, it is unable to describe an anharmonic part of the phonon spectra. A very useful formalism allowing exactly this is developed in Ref. [42].

At very low temperatures (well below Debye temperature) the upper limit of the integral in Equation 1.40 goes to infinity and we get the phonon contribution to specific heat as $c_{\mathrm{ph}}(T) \cong 234n\mathrm{R}(T/\theta_{\mathrm{D}})^3$ [26, Equation 5.32]. For a simple low-temperature experimental data evaluation we can therefore use the formula

$$c_{\mathrm{p}}(T) = c_{\mathrm{el}}(T) + c_{\mathrm{ph}}(T) = \gamma T + \beta T^3. \tag{1.41}$$

The magnetic contribution can be described in many ways. In a very simple case via the difference in configurational entropy, see Equation 1.30, between the magnetically ordered state and randomly oriented spin state as [43, Equation 16]

$$\Delta S_{\mathrm{mag}} = \mathrm{R} \sum p_i \ln(p_i) \tag{1.42}$$

where p_i is the probability of the system being in a microscopic state i. In the magnetically ordered state only one state exists ($p = 1 \rightarrow \Delta S_{\mathrm{mag}} = 0$) but in the randomly oriented spin state the total spin of each cation can be oriented equally in any of $2s+1$ directions (s is its spin quantum number) and therefore, assuming no spin coupling, we get

$$\Delta S_{mag} = \mathrm{R} \ln(2s + 1). \tag{1.43}$$

2. Experimental Details

2.1 Crystal Growth

One of the very common and industrially very important techniques used for growth of single crystals is the Czochralski process (Jan Czochralski, 1916, [44]). It is used during preparation of single crystals of semiconductors, like silicon or germanium, metals and many other compounds.

In principle a polycrystalline material of the highest available purity of a stoichiometric composition of the desired single crystal is placed in a crucible (made of copper for example). The polycrystalline material is then melted and once the melting is finished a seed of the desired crystal is introduced into the liquid in a vertical direction from the top. The tip of the seed melts in the liquid but a solid part of it is still attached on top. Afterwards the growing process itself can start via slow pulling of the solid crystal seed away from the liquid metal (semiconductor, ...). If the conditions of the experiment like the pulling speed of the seed or temperature of the liquid are well set during the pulling of the crystal seed new crystal grows on its bottom part from the melted metal and one gradually obtains an ingot of the desired single crystal. It should also be noted that the whole process is carried out while the crucible and the seed crystal are rotating in opposite directions and the whole growth is also carried out under protective atmosphere of, for example, argon gas.

2.2 Structural and Phase Analysis

For a proper analysis of an obtained sample a detailed knowledge of its microscopic structure is necessary. Since the size of the elementary unit cell is of the order of Ångströms ($1\text{Å} = 10^{-10}\text{m}$) techniques which are usually used for structural analysis on such scales are based on interference of waves diffracted from the periodically arranged structure, see Section 1.2. These waves can either be of an electromagnetic nature, i.e. light of different wave lengths, or of a particle nature, due to the wave–particle duality of particles. Depending on which probe, i.e. either electromagnetic radiation or a particle, one uses one can study different characteristics of the periodical arrangement (crystal). In this study diffraction of X-Ray waves and neutron particles was used and will be discussed.

An equally important part of a sample (crystal) analysis is the phase analysis in which the chemical composition of the sample is confirmed using for example (as in this study) a scanning electron microscope (SEM) equipped with an EDX spectroscopy option.

2.2.1 SEM & EDX

A scanning electron microscope is a device in which an interaction of an electron beam with the studied crystal is exploited. Electrons' wavelengths are much smaller when compared to visible light and they therefore allow us to study the topography of the crystal on a much smaller scales. An incident focused beam of electrons used in SEM also ejects electrons which are bound in individual atoms

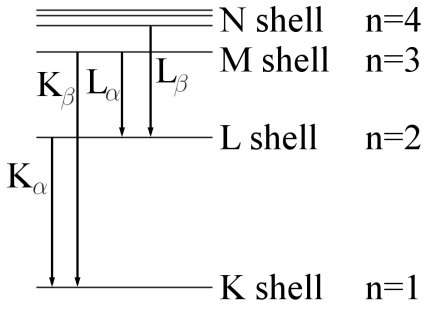

Figure 2.1: Illustration of a set of energy levels (shells) in an atom (labeled K for n=1, L for n=2 and so on) and possible characteristic energies of characteristic emitted photons (labeled K_α, K_β and so on).

of the sample from ground state creating a hole in the lower-energy shell. When then another electron from a higher-energy shell jumps into this empty ground state the positive energy difference will be released as a so-called characteristic X-Ray radiation, see Figure 2.1. An EDX (i.e. energy-dispersive X-ray spectroscopy) analyzer is then able to analyze intensity of this radiation depending on its energy (wavelength) producing a spectrum which is unique to atoms of every element. Analyzing this spectrum therefore gives us information about the chemical composition of the crystal and together with the knowledge of its real space distribution can help us estimate the homogeneity and composition of the studied sample.

In our study a scanning electron microscope (Mira I LMH, TESCAN) with an EDX detector (Bruker AXS) was used.

2.2.2 X-Ray Powder Diffraction

X-Ray diffraction is a method based on an interference of X-Ray radiation diffracted from the studied sample. Since X-Ray sources can be realized in quite compact sizes the use of X-Rays is very common and popular for characterizations in a small-size laboratories. The X-ray wavelength is of the order of Å, i.e. of the order of typical interatomic distances in a solid [45]. The X-Ray radiation obtained from small laboratory sources, e.g. X-Ray tube with a copper target, produce radiation of flux sufficient for a characterization of the structure of the studied sample.

For X-Ray powder diffraction experiments a very much used experimental arrangement is the Bragg-Brentano geometry, see Figure 2.2. The X-Ray radiation hits the studied crystal under specific angle θ and the afterwards diffracted radiation is detected only under angle 2θ. From the value of this specific angle θ the set of crystallographic planes from which the radiation was diffracted can be calculated. The measurement is carried out for various values of θ and the obtained data – angle dependence of the diffracted intensity $I(\theta)$ – is then the specific spectrum of the studied structure. In order to obtain, confirm or refine a crystal structure from such an experiment we have to be able to describe the experimental data with an appropriate model. This usually means that some basic information about the structure (i.e. its space group, lattice parameters,

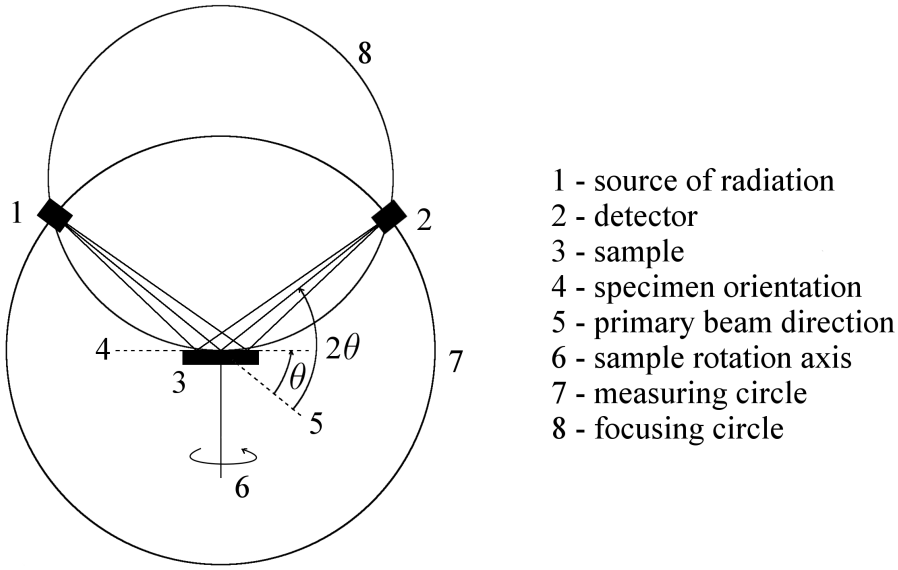

Figure 2.2: Bragg-Brentano geometry of an X-Ray powder diffraction experiment.

fractional coordinates of the present atoms, ...) has to be known in advance and is then only refined via comparison of the calculated profile with the experimental data.

In our study the X-Ray powder diffraction experiments were carried out at the Department of Condensed Matter Physics of Charles University in Prague using the powder diffractometer Bruker D8 Advance [46].

The Rietveld Method

To analyse the X-Ray powder diffraction patterns the FullProf Suite [47, 40] was used in this study. The techniques used are based on the so-called Rietveld analysis [48, 49], i.e. a profile refinement method of powder diffraction data.

The measured pattern is given as two arrays $\{2\theta_i, y_i\}_{i=1,\dots,n}$ (y_i denotes counts) and the modelled profile at the ith step is calculated as a sum of neighbouring Bragg diffractions and a background [47, FullProf Manual, Equation 3.1]

$$y_{c,i} = \sum_{\phi} S_\phi \sum_{\mathbf{g}} I_{\phi,\mathbf{g}} \Omega(2\theta_i - 2\theta_{\phi,\mathbf{g}}) + b_i. \tag{2.1}$$

ϕ denotes the phase, S_ϕ the scale factor, $\mathbf{g} = \mathbf{G}$ the Bragg diffractions, $I_{\phi,\mathbf{g}}$ the integrated intensities, Ω diffraction profile function and b_i the counts from the background. The Rietveld Method then consists of refining a crystal structure by minimising the weighted squared difference between the observed $\{y_i\}_{i=1,\dots,n}$ and calculated pattern $\{y_{c,i}\}_{i=1,\dots,n}$ against parameter vector $\alpha = (\alpha_1, \alpha_2, \cdots, \alpha_p)$. The parameter vector contains all structural variables (specified by user) which are available for fitting. The integrated intensities are generally calculated as [47,

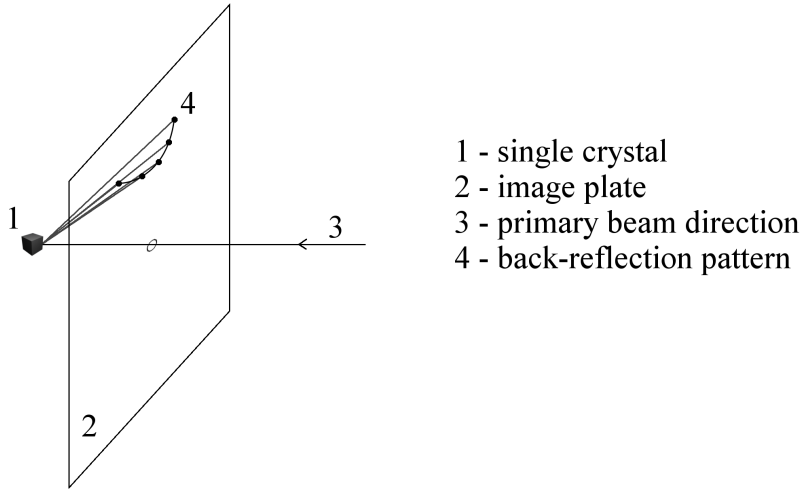

Figure 2.3: Back-reflection arrangement for the Laue method.

FullProf Manual, Equation 3.2]

$$I_{\phi,\mathbf{g}} = \{LAPCF^2\}_{\phi,\mathbf{g}} \tag{2.2}$$

where $L_{\mathbf{g}}$ contains the Lorentz, polarisation and multiplicity factors, $A_{\mathbf{g}}$ is the absorption coefficient, $P_{\mathbf{g}}$ is the preferred orientation function, $C_{\mathbf{g}}$ includes special correlations and $F_{\mathbf{g}}$ is, of course, the structure factor.

2.2.3 Laue Diffraction

Laue method is another diffraction technique which is very much used in the presented study. In this method the studied single crystal is irradiated with a collimated polychromatic X-Ray radiation and the consequently diffracted radiation is detected on a 2D planar image plate which is perpendicular to the primary beam direction. Both the sample and the primary beam directions are fixed throughout the whole experiment so for each set of crystallographic planes hkl the Bragg angle θ is fixed. Since the used incident X-Ray waves are polychromatic the Bragg law (Equation 1.14) is satisfied for more θ and there are many diffractions (belonging to various hkl planes) visible on the image plate. It should also be noted that because of the use of polychromatic waves the image of the reciprocal lattice is distorted. However, the big advantage of this technique is that it gives us the image in quite a short time and is therefore very useful for not only determination of basic symmetries in the studied single crystal but also for the process of finding principal crystallographic directions, which is a necessity for consequent measurements of anisotropic material properties. The so-called back-reflection arrangement for the Laue method used in this study is displayed in Figure 2.3.

2.2.4 Neutron Diffraction

Neutron diffraction is a method based on an interference of a beam of neutron particles diffracted from the studied sample. The nature of neutron diffraction

experiments is in principle similar to the X-Ray diffraction experiments, however, there is a number of crucial differences stemming from the fact that the used probes are neutrons instead of X-Rays. Using formula for the de Broglie wavelength $\lambda = h/p$ of a matter wave of a particle with momentum p written as $p = \hbar k$ and the relation between the energy and mass m of a particle $E = \hbar^2 k^2/2m$ one can approximate the neutron wavelength as

$$\lambda(\text{Å}) \cong \frac{0.29}{\sqrt{E(\text{eV})}}. \tag{2.3}$$

For neutrons with energy of 0.08 eV we then get the wavelength of 1Å, i.e. as in the case of X-Ray radiation of the order of typical interatomic distances in a solid [45].

In our neutron diffraction experiments the single-crystal four-circle diffractometer with three-axis energy analysis (D10) at the Institut Laue-Langevin (ILL) in Grenoble (France) was used. Its instrumental layout is displayed in Figure 2.4. In principle, the studied sample placed in a four circle dilution cryostat is irradiated with a beam of neutrons of a given wavelength in a specific direction and the consequently diffracted beam is detected by an analyser. The monochromator selects (separates) neutrons of the given wavelength from the neutron guide, the monochromatic beam then passes through slits which limit its size and consequently irradiates the sample. The sample is placed in an Eulerian cradle with three axes ω, χ and ϕ which allow rotation of the sample until a given set of atomic planes hkl diffract the neutron beam into the equatorial plane and the diffracted beam is then detected by an analyser which can rotate around the sample within the equatorial plane. By specifying the direction of incident and diffracted beam a certain Bragg diffraction maxima hkl can be chosen and intensity can be recorded. After recording intensities of a number of diffractions the structure of the studied crystal can be obtained [50].

2.3 Physical Property Measurement System

For characterization of basic thermodynamic, transport and magnetic properties of the studied compounds we performed experiments at the Joint Laboratory for Magnetic Studies [51] of Department of Condensed Matter Physics of Charles University and the Institute of Physics of The Czech Academy of Sciences using a Physical Property Measurement System [52] with 9(14)T superconducting coil from Quantum Design Inc. It is a variable system which allows experiments in magnetic fields up to 14T and at temperatures down to 0.35K measuring various physical properties (depending on which of the many options is used). In our study it was used for experiments measuring specific heat, electrical resistivity and magnetization (using vibrating sample magnetometer) of the studied compound.

2.3.1 Specific Heat

Measurements of specific heat at constant pressure, see Equation 1.29, have been performed using QD Heat Capacity option. The experimental arrangement is as follows: A sample is fixed on a platform with a thin layer of Apiezon N grease,

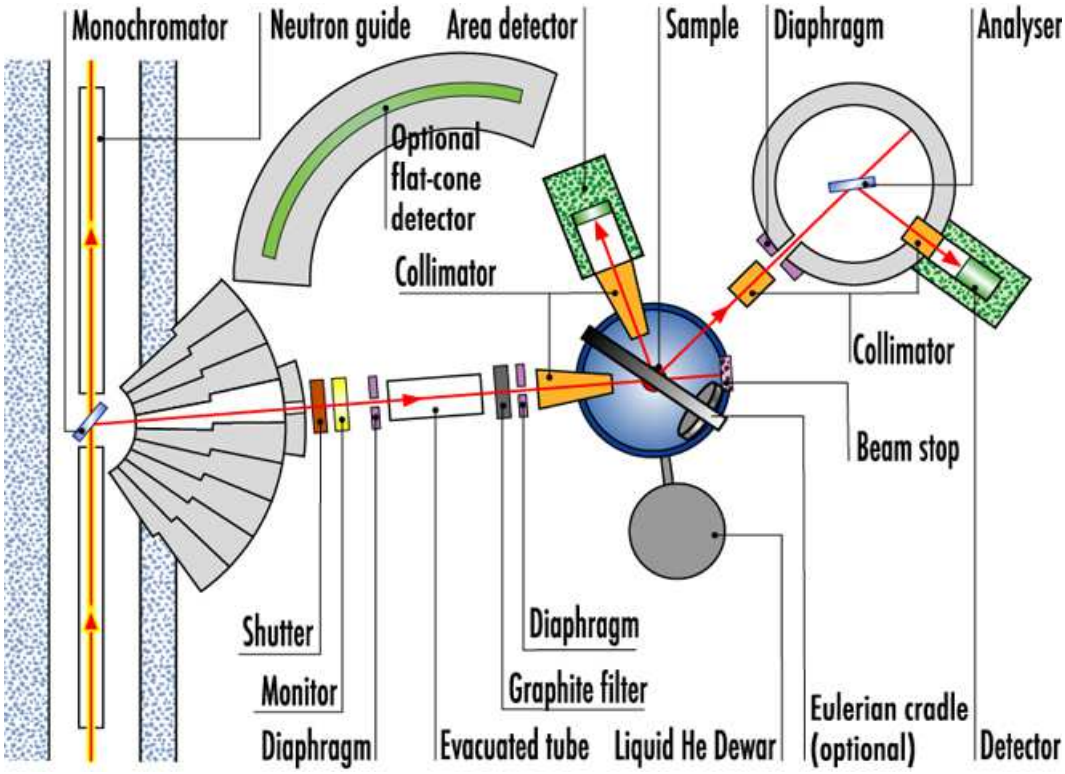

Figure 2.4: Instrumental layout of the single-crystal four-circle diffractometer with three-axis energy analysis (D10) [50].

the platform is equipped with a thermometer and a heater and is connected to a thermal bath (a puck) via small connecting wires. These serve as both electrical and thermal connection and mechanical support. The ambient space is pumped to such a vacuum that the wires are the main heat link between the bath and the platform. The heater is then able to supply a controlled amount of heat to the platform while the thermometer monitors the resulting change in temperature. Schematic layout is displayed in Figure 2.5 [53].

The experiment itself is then consisting of two phases: a heating period during which a known amount of heat is applied at constant power for a specific time and then a cooling period during which the temperature relaxes. Temperature of the platform is monitored during both phases and the whole temperature response (time dependence of temperature) is then fitted to a appropriate model

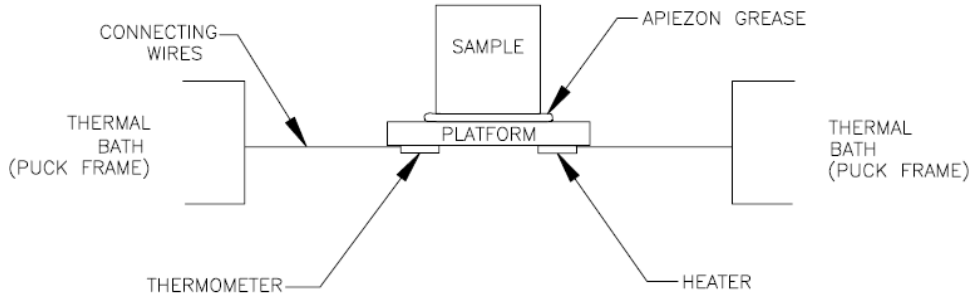

Figure 2.5: Experimental layout of PPMS Heat Capacity Option [53].

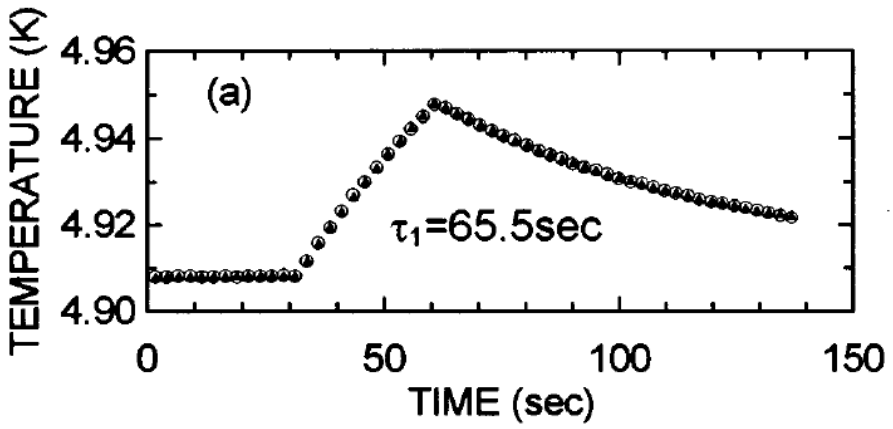

Figure 2.6: Time dependence of platform temperature of 0.24976g copper as published in Ref. [54], circles represent measured points, triangles fitted points and τ_1 is a time constant used to characterize the equilibrium between the sample platform and the bath.

as described in Ref. [54]. The model accounts for the thermal relaxation of the sample platform to the bath as well as the sample platform to the sample itself, the result of such fitting is displayed in Figure 2.6. Performing such an experiment with the consequent fitting at various temperatures (and magnetic fields) then give us the desired temperature (magnetic field) dependence of specific heat.

Experiments which have been carried out in Ref. [55] conclude that the PPMS system manufactured by QD exhibits an overall accuracy better than 1% for temperatures between 100K and 300K while the accuracy diminishes at lower temperatures. The obtained data confirm that the system operates within the 5% accuracy specified by QD and measurements on gold samples with masses of 4.5mg and 88mg indicate that accuracy of 3% or better can be achieved below 4K by using samples with heat capacities that are half or greater than the calorimeter addenda heat capacity.

2.3.2 Electrical Resistivity

Resistivity can be determined with a very good precision using the so-called 4-point method. Experimental arrangement is schematically plotted in Figure 2.7. A sample of the studied material is cut into a rectangular cuboid of known cross-section dimensions a, b and afterwards contacted with 4 wires arranged linearly along the third dimension of the sample. The two outer probes pass electric current I through the sample while the inner two probes measure the induced voltage U. If the distance between inner probes is d then the resistivity ρ can be calculated using the trivial formula

$$\rho = \frac{a \cdot b}{d} \frac{U}{I}. \tag{2.4}$$

The main advantage of this technique stems from the fact that the voltmeter has a very high resistance and therefore the inner wires draw little to no current eliminating (almost) the inaccuracies caused by resistance of the contacts and the

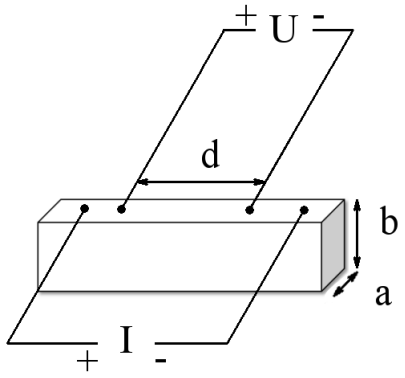

Figure 2.7: Experimental layout of 4-point AC resistivity measurement.

wiring. In the presented measurements the sample has been glued on a suitable puck with the insulating GE Varnish, contacted using gold wires with a diameter of 25μm and then placed in the PPMS cryostat.

2.4 Magnetic Property Measurement System

For experiments measuring magnetization under various conditions a MPMS XL 7T (Magnetic Property Measurement System) present at Magnetism and Low Temperature Laboratories (MLTL) [56] of Department of Condensed Matter Physics of Charles University has been used. It allows very precise experiments in magnetic fields up to 7T and temperatures down to 1.9K exploiting the sensitivity of a Superconducting QUantum Interference Device (SQUID) magnetometer.

A SQUID combines the physical phenomena of flux quantization and Josephson tunnelling. It is able to detect a change in applied magnetic flux corresponding to a tiny fraction of one flux quantum, in today's devices typically 10^{-6} ϕ_0 $\mathrm{Hz}^{-1/2}$. SQUIDs – which are intrinsically flux-to-voltage transducers – are the most sensitive detectors of magnetic flux known [57].

3. Results

3.1 Crystal Growth

A single crystal of $CeCo_{0.715}Si_{2.285}$ labelled JM004 has been successfully grown by a modified Czochralski pulling method, see Section 2.1. The experiment was carried out under a high-purity argon atmosphere (99.9999%) in a triarc furnace which uses electric arcs for melting the polycrystalline material in a water-cooled copper crucible and is available at the Technology Lab of Department of Condensed Matter Physics of Charles University [58]. Pulling speed of 6mm/h has been used together with rotation speed 2rpm of the crucible and 2rpm of the counter-rotating seed. The growth was carried out from an off-stoichiometric composition of Ce : Co : Si = 1 : 1 : 3.5 of high-purity elements (99.9% Ce, further purified by solid state electrotransport [59], 99.995% Co and 99.9999% Si) and using a seed made of a wolfram rod.

In order to minimize the amount of defects in the crystal lattice an annealing process was carried out on the crystals from a JM004 growth – the obtained ingot was wrapped in a tantalum foil (99.9%), sealed in a quartz tube and annealed at 900°C for one week under vacuum of 10^{-9}bar.

A second successful growth of $CeCo_{0.715}Si_{2.285}$ labelled JM018 was carried out under the same conditions (same initial composition, same pulling and rotation speeds, same purity of elements) only using a piece of JM004 crystal instead of a wolfram rod as a seed. The obtained ingot can be seen in Figure 3.1. Since at the time of the second growth it was already clear from preliminary neutron diffraction experiments (see Section 3.5) that JM004 is not a single-grain crystal we did not perform any annealing processes on the JM018 in order to minimize the chance of obtaining a multi-grain crystal.

3.2 Crystal Structure and Phase Analysis

The crystal structure of the studied novel compound $CeCo_{0.715}Si_{2.285}$ at room temperature was determined via single crystal X-Ray diffraction experiments performed by I. Císařová from Department of Inorganic Chemistry, Faculty of Science of Charles University in Prague. The structure was obtained from an

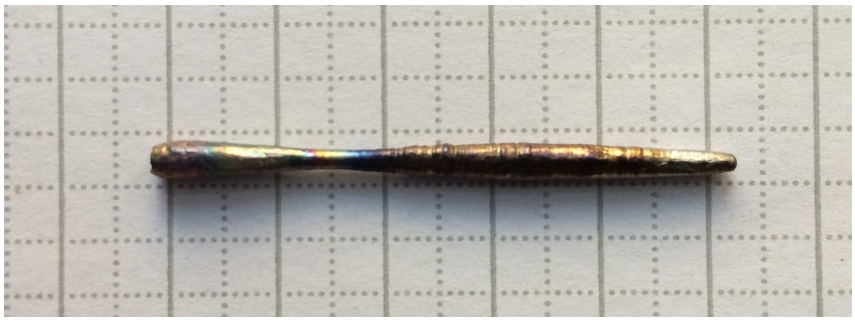

Figure 3.1: The JM018 ingot of $CeCo_{0.715}Si_{2.285}$ grown by Czochralski process in a triarc furnace. The dotted lines on the underlying surface are in 5mm distance.

experiment during which 517 diffractions (305 independent) were measured using characteristic Mo K_α X-Ray radiation. The compound crystallizes in the *I-4m2* (Nr. 119) space group structure with a unit cell which is extremely elongated along [001] direction – lattice parameters $a = b = 4.13$Å and $c = 32.84$Å. The structure is tetragonal and noncentrosymmetric, information about the unit cell is summarized in Table 3.1 including fractional coordinates of atoms, multiplicities and Wyckoff position letters of individual atom sites and occupancies of the atoms. The structure is also plotted in Figure 3.2.

Atom label	**Atom**	**x**	**y**	**z**	**Multiplicity and Wyckoff letter**	**Occupancy**
Ce1	Ce	0	0	0	2a	1/8
Ce2	Ce	0	0	0.644	4e	1/4
Ce3	Ce	0	0.5	0.25	2a	1/8
Co1	Co	0	0	0.106	4e	1/4
Co2	Co	0	0	0.54	4e	$1/4 \cdot 0.43$
Si1D	Si	0	0	0.53	4e	$1/4 \cdot 0.57$
Si1	Si	0	0.5	0.715	4f	1/4
Si2	Si	0	0.5	0.573	4f	1/4
Si3	Si	0	0	0.176	4e	1/4
Si4	Si	0	0.5	0.073	4f	1/4

Table 3.1: Detailed information about unit cell of the studied $CeCo_{0.715}Si_{2.285}$ compound, x, y and z are the fractional coordinates of atoms.

To further confirm the above–described crystal structure X-Ray powder diffraction experiments, see Section 2.2.2, were performed on numerous pieces from various parts of JM004 and JM018 ingots. Rietveld refinement, see Section 2.2.2, was carried out using the experimental data. The agreement was acceptable – R_F factor usually approximately 15 – but more importantly no foreign phase diffraction peaks were observed.

To obtain further information about the phase purity of the studied crystals experiments using a scanning electron microscope equipped with an EDX spectroscopy option were carried out, see Section 2.2.1. On a well polished straight plane of samples of our crystal numerous EDX spectra were obtained and analysed including their spatial distribution (one dimensional – a so-called line scan or two dimensional – a mapping) from which the spatial distribution of the present atoms was derived. Typical results of EDX spectra analysis are summarized in Table 3.2 for both JM004 and JM018. The results obtained for JM018 are (within the margin of error) in agreement with the composition of $CeCo_{0.715}Si_{2.285}$ while in the case of JM004 the results systematically differed from the $CeCo_{0.715}Si_{2.285}$ composition – this is well seen in line scan measurements, a typical one is displayed in Figure 3.3. The amount of cobalt is overestimated while the amount of silicon is underestimated. Many mapping measurements were also carried out, all showed a very good homogeneity of the samples used for further measurements of physical properties, result of a typical mapping measurement (on either JM004 or JM018) is displayed in Figure 3.4.

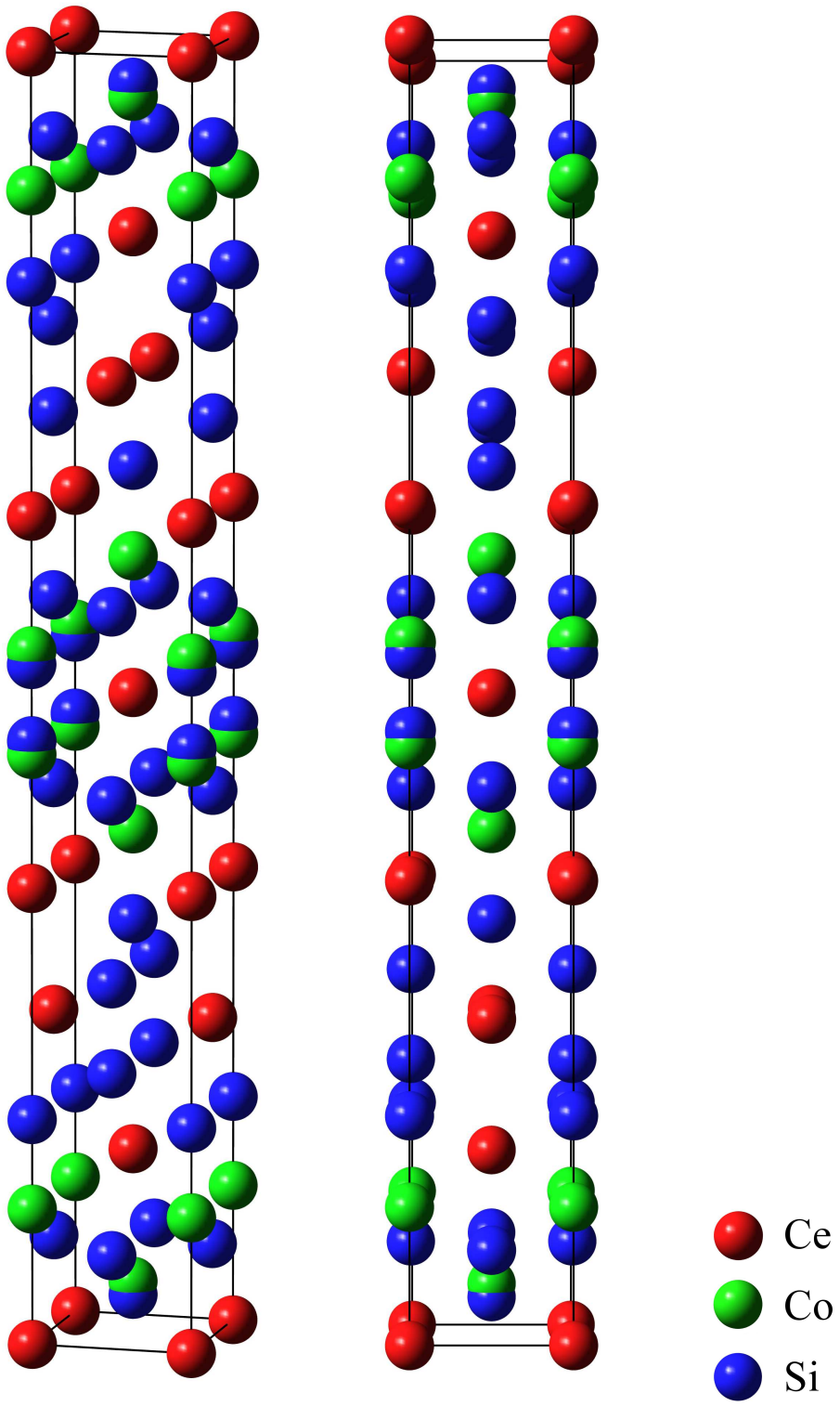

(a) (b)

Figure 3.2: (a) Structure of $CeCo_{0.715}Si_{2.285}$ as determined by I. Císařová, (b) the same structure viewed from [100] direction.

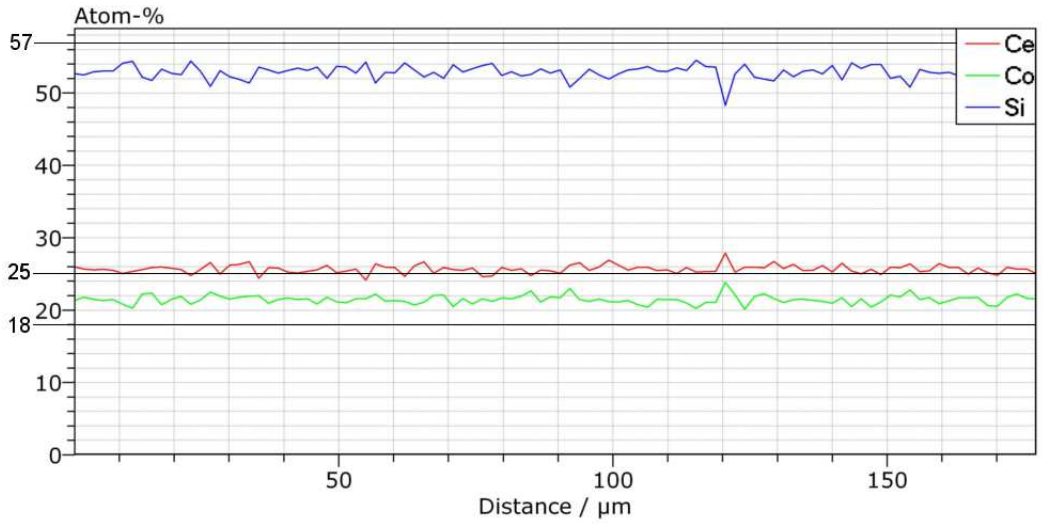

Figure 3.3: A distribution of Ce, Co and Si elements in $CeCo_{0.715}Si_{2.285}$ crystal JM004 along a real space line obtained from a SEM/EDX measurement. Relative concentration expected for $CeCo_{0.715}Si_{2.285}$ is marked on the vertical axis.

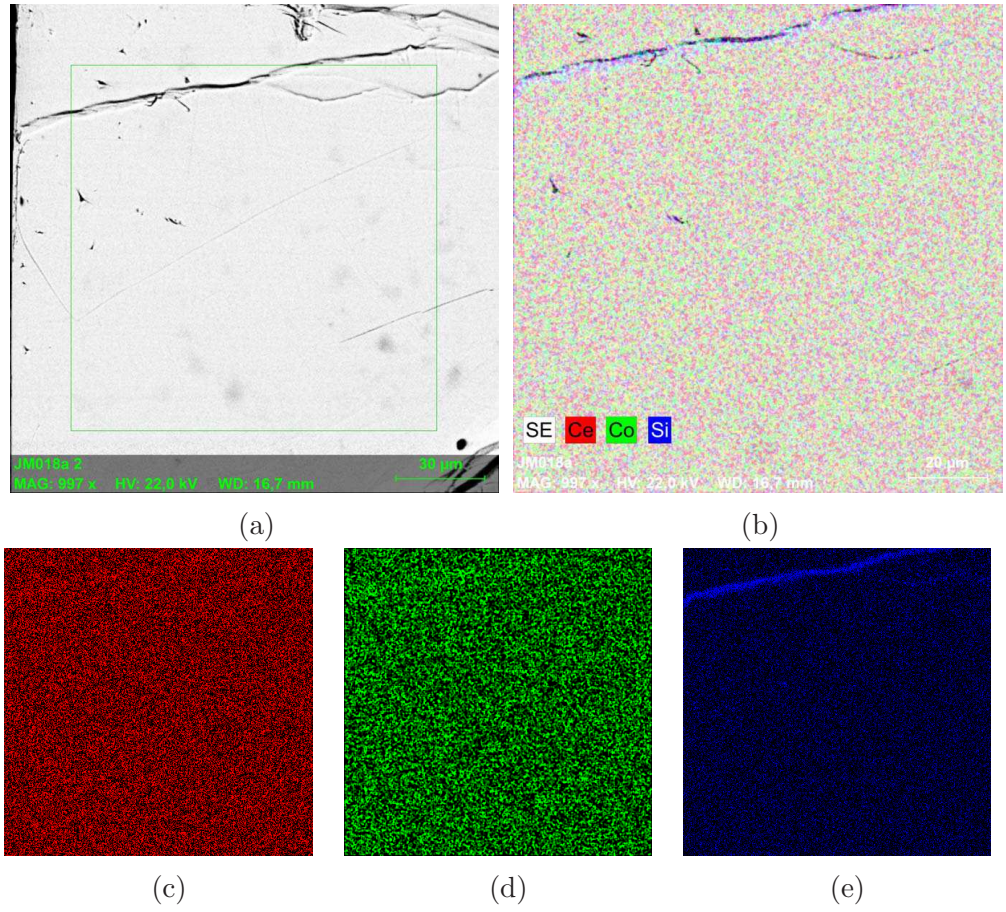

(a) (b)

(c) (d) (e)

Figure 3.4: Result of a SEM/EDX mapping measurement on JM018a sample. (a) microscopic picture of the surface, (b) spatial distribution of Ce, Co and Si elements and of only (c) Ce, (d) Co or (e) Si.

Element	Series	norm. C [wt.%]	Atom C. [at.%]	Error [%]	$CeCo_{0.715}Si_{2.285}$ [at.%]
JM004					
Cerium	L-series	57.03	**25.98**	1.5	**25.00**
Cobalt	K-series	19.87	**21.52**	0.5	**17.88**
Silicon	K-series	23.10	**52.51**	1.0	**57.13**
JM018					
Cerium	L-series	56.21	**24.41**	1.6	**25.00**
Cobalt	K-series	17.00	**17.56**	0.5	**17.88**
Silicon	K-series	26.78	**58.03**	1.2	**57.13**

Table 3.2: Typical results of EDX spectra analysis of JM004 and JM018 crystals.

For further measurements of physical properties samples of single crystals of suitable shapes have been separated from the ingots using a fine wire saw for cutting and Laue method, see Section 2.2.3, for a search for single crystals as well as for determination of their orientation. To be as sure as possible (within the limitations of available techniques) that our samples are single-grain we have also measured a series of lauegrams (Laue diffraction patterns) while rotating the sample around [100] axis, the whole series of patterns (together with simulated ones) of JM018a sample is displayed in Figure 3.5. A slight misalignment of the experimental data with the simulated pattern is unimportant since the purpose of the experiment was the evaluation of 'single–crystallinity' of the sample.

3.3 Thermodynamic and Transport Properties

For thermodynamic characterization of the studied $CeCo_{0.715}Si_{2.285}$ compound temperature dependence of its specific heat at constant pressure was measured using the relaxation calorimetry as described in Section 2.3.1. Results are displayed in Figure 3.6 for both JM004 and JM018 crystals. At high temperatures a typical Debye behaviour is observed, see Equation 1.40. At low temperatures, however, the JM004 exhibits two anomalies, at $T'_N = 10.7$K and at $T^* = 9.8$K, while the JM018 only one at $T_N = 10.0$K. The phase transition temperatures were estimated as the points where the derivative with respect to temperature reaches its maximum. For JM018 we also show results of experiments with applied external magnetic field $H||[001]$, the transition is shifted to higher temperatures in fields up 2T.

The least-squares fitting of a linear dependence to C/T vs. T^2 data, according to Equation 1.41, in a low temperature region (below the ordering temperature) provides a value of Sommerfeld coefficient of $\gamma' = 29\text{mJ/molK}^2$ and $\gamma = 34\text{mJ/molK}^2$ for JM004 and JM018, respectively.

As the non-magnetic analogue is not available for this compound, in order to estimate the magnetic entropy connected to the observed transitions we subtracted the part not related to the long range magnetic order by approximating the 'background' by a smooth curve (specifically by a polynomial of 6^{th} degree), see Figure 3.6. Via a numerical integration of the difference we were then able

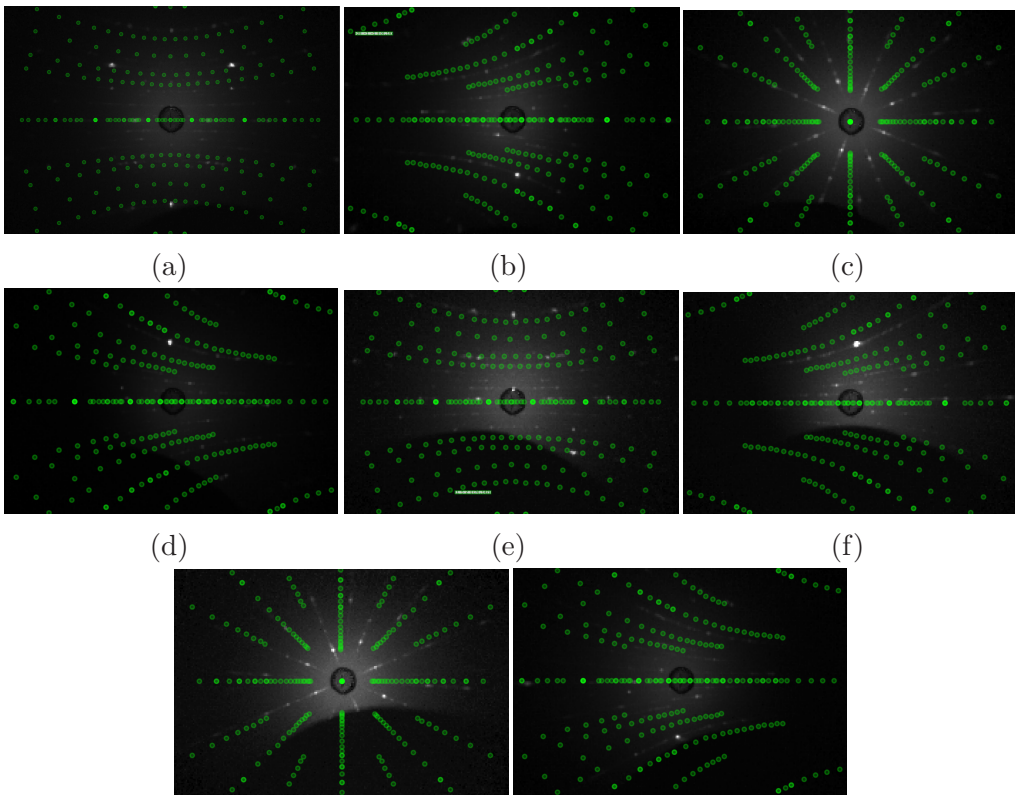

Figure 3.5: A series of lauegrams of $CeCo_{0.715}Si_{2.285}$ sample JM018a measured while rotating the sample around [100] axis, each pattern (a)-(h) differs from the previous one by a rotation by an angle $\pi/2$. (a), (e) Single crystal diffraction patterns in [010] direction; (c), (g) in [001] direction. The green circles represent simulated patterns for the appropriate structure and direction.

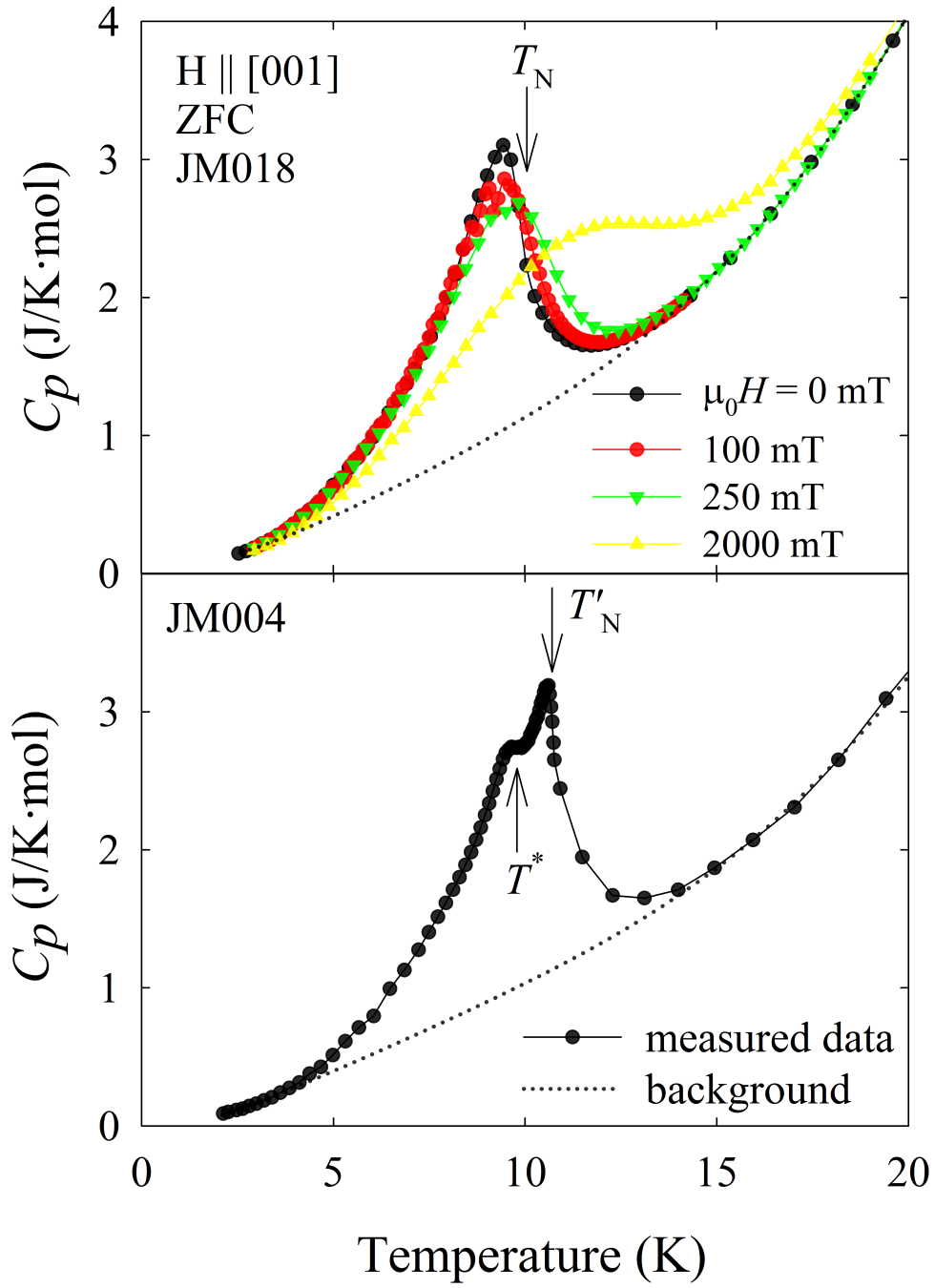

Figure 3.6: Temperature dependence of specific heat of $CeCo_{0.715}Si_{2.285}$ crystals JM004 and JM018 at low temperatures, including an approximation of the 'background' (which is not related to the long range magnetic order).

to estimate the change in magnetic entropy associated with magnetic ordering as $\Delta S' = 0.78\text{J/molK} = 0.14\text{Rln2}$ and $\Delta S = 0.79\text{J/molK} = 0.14\text{Rln2}$ for JM004 and JM018 respectively, values are compared with Equation 1.43 for $s = 1/2$ of Ce^{3+}.

Using the 4-point method, see Section 2.3.2, the temperature and magnetic field dependence of electrical resistivity has been estimated, results are displayed in Figure 3.7 and Figure 3.10. The anomaly at T_N (T'_N) visible in specific heat data is observed in electrical resistivity as well, see insets in Figure 3.7. In the case of JM018 crystal, we observe a sharp drop of resistivity at the magnetic ordering temperature $T_N = 10.0\text{K}$, the dependency is isotropic. Similar behaviour is observed in the case of JM004 crystal with current applied in the basal plane, however, the electrical resistivity of this crystal is anisotropic and for current applied along c-axis ($J||[001]$) we observe different behaviour. Firstly, we observe a shallow maximum at approximately 290K and, secondly, below the ordering temperature $T'_N = 10.7\text{K}$ the resistivity increases, see inset in Figure 3.7.

First measurements of electrical resistivity under external hydrostatic pressure were carried out by J. Prokleška. The obtained temperature dependencies were similar to the one at atmospheric pressure, see Figure 3.7, only the magnetic ordering anomaly was shifted continuously to lower temperatures, the obtained evolution of the ordering temperature T'_N with pressure is displayed in Figure 3.8. Assuming the typical phase diagram of cerium-based ternary compounds, such as the one in Figure 2a, we speculate that the magnetism might be suppressed at pressures of approximately 6–7GPa, see inset in Figure 3.8.

3.4 Magnetic Properties

Using MPMS, see Section 2.4, or PPMS with VSM option, see Section 2.3, we have thoroughly studied magnetization (and susceptibility) of the $CeCo_{0.715}Si_{2.285}$ under various conditions, i.e. various magnetic fields and temperatures. The magnetic ordering at $T_N = 10.0\text{K}$ and $T'_N = 10.7\text{K}$ is manifested as an inflection point in temperature dependence of magnetization in small magnetic fields in both JM004 and JM018 crystals, see Figure 3.9 for JM004. To determine the nature of the ordered state below T_N measurements of magnetization curves at low temperatures in low fields were performed, results at 1.8 K are plotted in Figure 3.10 together with field dependence of electrical resistivity. Below T_N the compound exhibits a strong hysteresis of magnetization with respect to varying magnetic field or temperature (see Figure 3.9) as well as a strong anisotropy with easy axis corresponding to the [001] direction. The magnetization is almost unchanged above 1T and changes only slightly linearly up to 7T. Experiments at higher fields by D. Gorbunov show that the magnetization of JM018 is almost unchanged above 1T and increases only slightly linearly up to $0.3\mu_B$/Ce at 45T for $H||[001]$ and for $H||[100]$ (hard magnetization axis) magnetization increases non-linearly up to 35T at which it equals to the magnetization with $H||[001]$ and the both curves then continue together up to 45T[1]. The saturated value of magnetization at 1T is considerably reduced – $0.26\mu_B$/Ce for JM004 and $0.21\mu_B$/Ce for JM018 – with respect to the free Ce^{3+} ion value of saturated magnetic moment

[1] D. Gorbunov, personal communication

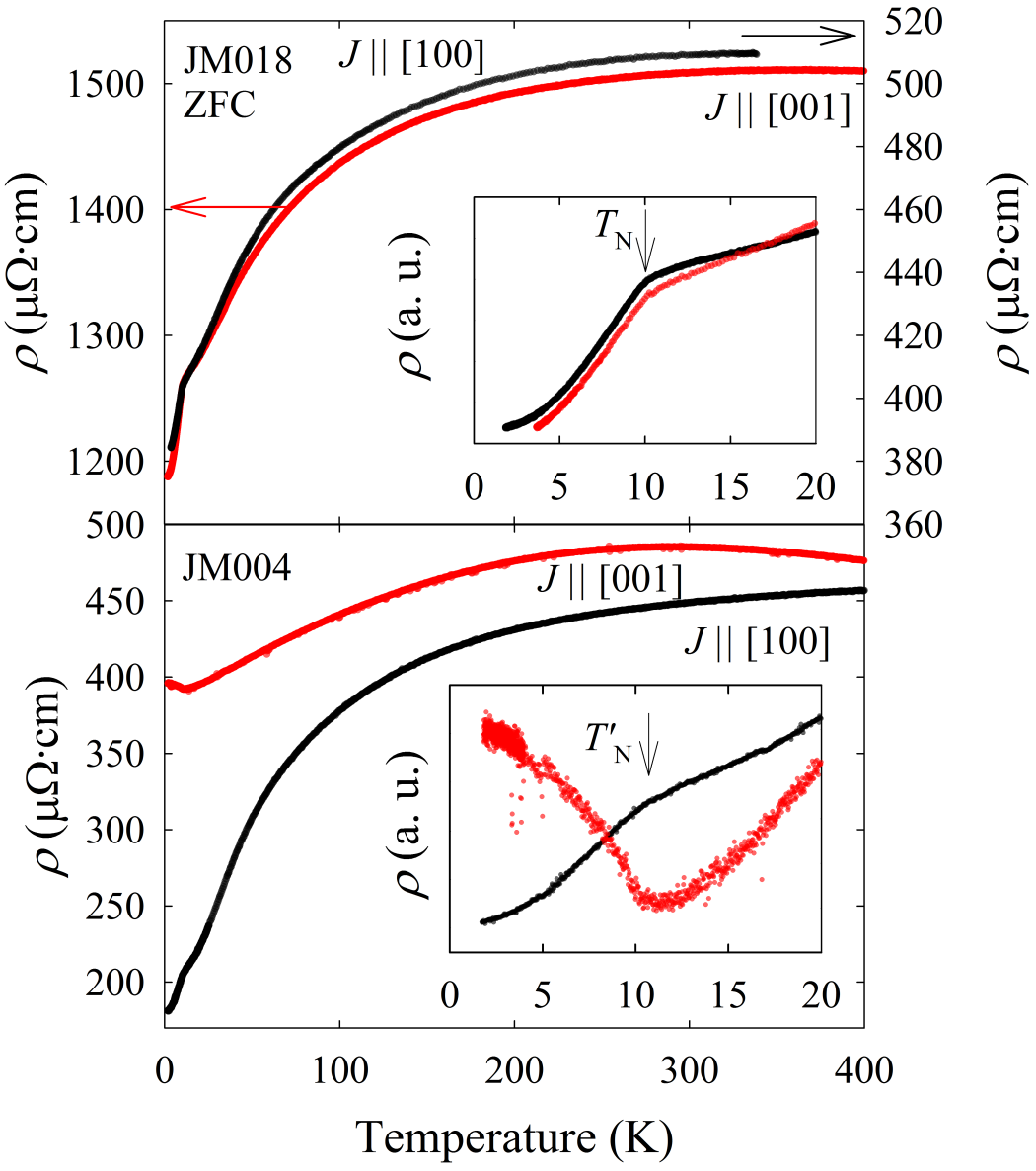

Figure 3.7: Temperature dependence of electrical resistivity in zero magnetic field of $CeCo_{0.715}Si_{2.285}$ with electric current applied in both J||[100] and J||[001] direction.

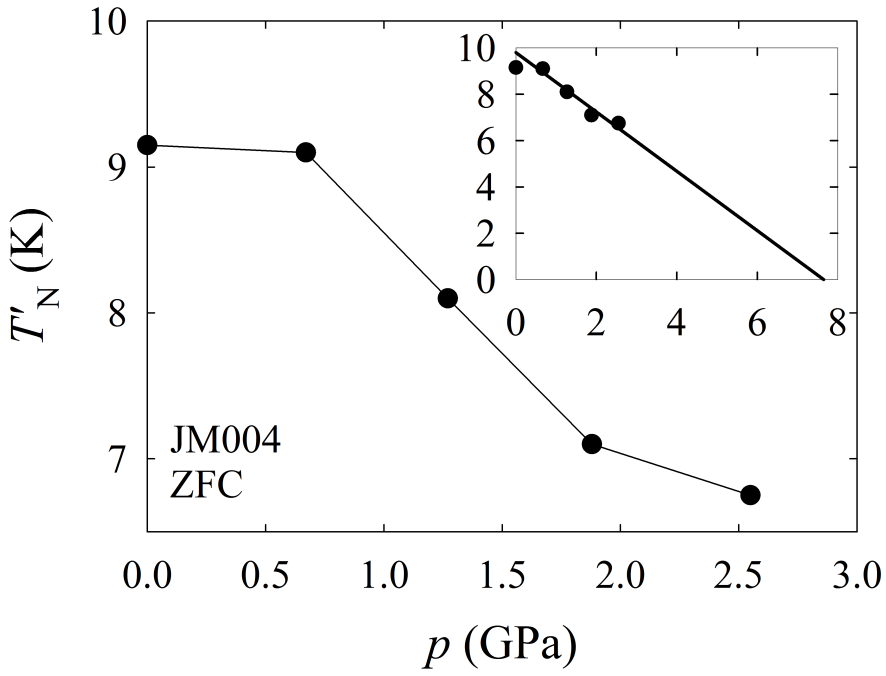

Figure 3.8: Evolution of the ordering temperature T'_N of the JM004 crystal of $CeCo_{0.715}Si_{2.285}$ with pressure.

$\mu \simeq 2.14\mu_B$, see Equation 1.5.

Besides, the compound exhibits quite interesting behaviour in small magnetic fields below 0.5T. As can be seen in Figure 3.11, the compound undergoes numerous magnetic phase transitions when magnetic field is applied in $H||[001]$ direction. Below the temperature of 11.0K firstly two phase transitions appear at 34mT and 18mT (for JM004). Further on, with decreasing temperature the transitions shift to higher magnetic fields and new transitions appear. At temperatures below 2.5K the number of transitions is again reduced while still being shifted to higher magnetic fields. As shown in Figure 3.10 the numerous magnetic phase transitions are also manifested in magnetic field dependence of electrical resistivity, however, the step-like behaviour is more pronounced in the magnetization data.

As shown in Figure 3.12, at high temperatures (200K $\leq T \leq$ 350K) temperature dependence of magnetic susceptibility of $CeCo_{0.715}Si_{2.285}$ can be fitted by the Curie-Weiss law, see Equation 1.2. It should, however, be stated that a small but non-negligible deviation of the data is observed at high temperatures with field $H||[001]$ for JM004 crystal. Least-squares fits of the Curie-Weiss law for magnetic field applied in [001] direction yield effective magnetic moments of $\mu_{\rm eff}^{||c\prime} = 2.8\mu_B$/Ce and $\mu_{\rm eff}^{||c} = 2.55\mu_B$/Ce and paramagnetic Curie-Weiss temperatures of $\theta_{\rm p}^{||c\prime} = -276$K and $\theta_{\rm p}^{||c} = -263$K of JM004 and JM018 crystals respectively. For field applied in [100] direction the effective magnetic moment is $\mu_{\rm eff}^{||a\prime} = 3.97\mu_B$/Ce and $\mu_{\rm eff}^{||a} = 3.47\mu_B$/Ce and paramagnetic Curie-Weiss temperature $\theta_{\rm p}^{||a\prime} = -928$K and $\theta_{\rm p}^{||a} = -766$K respectively. In comparison to the value of effective magnetic moment of the free Ce^{3+} ion $\mu_{\rm eff} \simeq 2.54\mu_B$, see Equation 1.5, the values of the moment are unrealistic and the behaviour can not be described using the Curie-Weiss model. Still, the large negative values of the paramagnetic

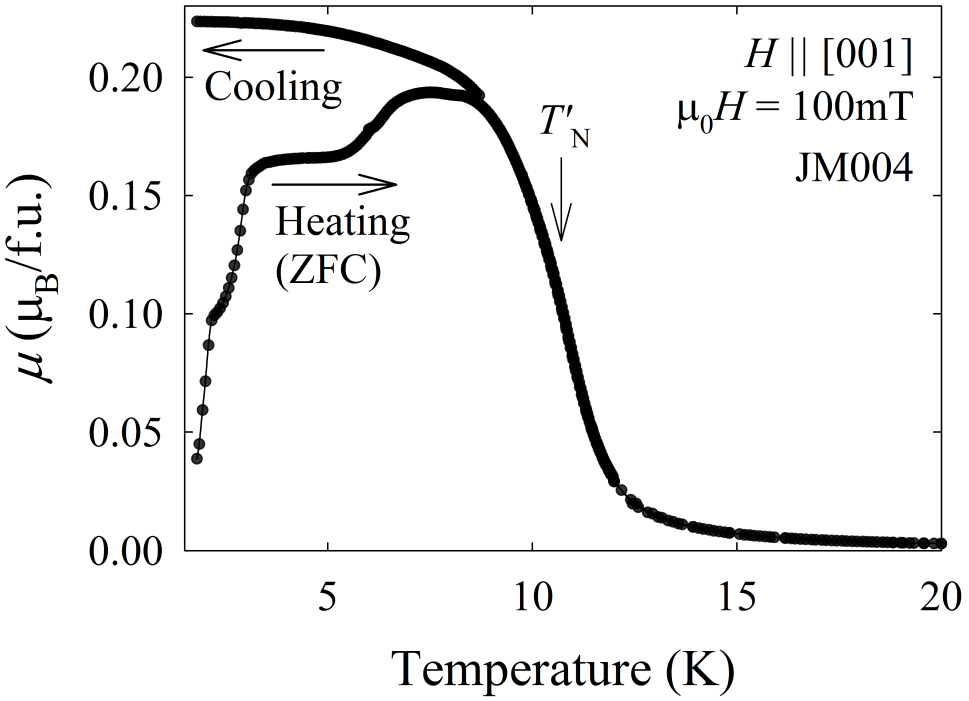

Figure 3.9: Temperature dependence of magnetization of $CeCo_{0.715}Si_{2.285}$ crystal JM004 in small magnetic field showing thermal hysteresis.

Curie-Weiss temperature θ_p show predominance of antiferromagnetic interactions.

3.5 Magnetic Structure

The magnetic structure was determined via single crystal neutron diffraction experiments, see Section 2.2.4, in cooperation with Milan Klicpera and Bachir Ouladdiaf from ILL. Firstly, some preliminary diffraction experiments were carried out using a Laue single crystal diffractometer CYCLOPS in order to select a truly single grain crystal and orient it for further measurements. The investigation confirmed good crystallinity of the sample, from experiments at low temperatures first estimations of the propagation vector of the $CeCo_{0.715}Si_{2.285}$ compound were made.

Experiments on the D10, see Figure 2.4, were then performed. After properly installing and orienting the sample in the instrument we searched for the propagation vector by performing scans along certain lines in the reciprocal space, see Section 1.2.1, at temperatures well above ($T = 20$K) and well below ($T = 1.5$K) the ordering temperature $T_N = 10.0$K. Such scans were performed along $[00l]$ with $l \in \langle 1.0; 10.0\rangle$; $[h00]$ with $h \in \langle 0.5; 2.5\rangle$; $[hh0]$, $[hhh]$ and $[h0h]$ with $h \in \langle 0.5; 1.5\rangle$ and $[12l]$ with $l \in \langle 3.0; 11.0\rangle$. Since intensities of nuclear and magnetic diffractions are additive one is able to determine which diffractions are from the magnetic structure by comparing the spectra above and below the magnetic ordering temperature. Unfortunately, since the size of the cerium magnetic moments of the studied compound is significantly reduced, see Figure 3.10, the intensities

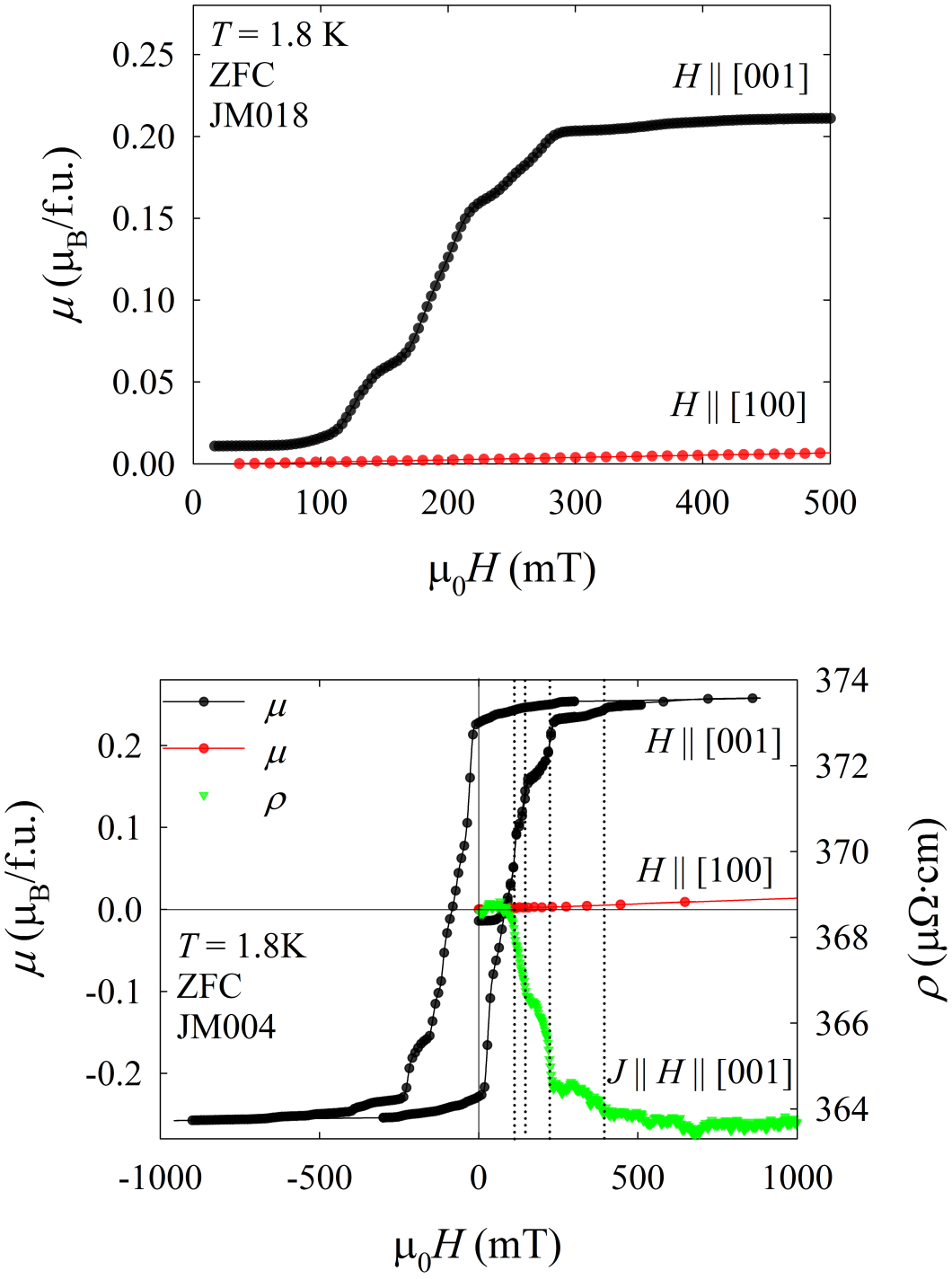

Figure 3.10: Magnetic field dependence of magnetization of $CeCo_{0.715}Si_{2.285}$ crystals JM004 and JM018 at 1.8K with field applied in both [100] and [001] direction. Field dependence of electrical resistivity of JM004 is shown as well.

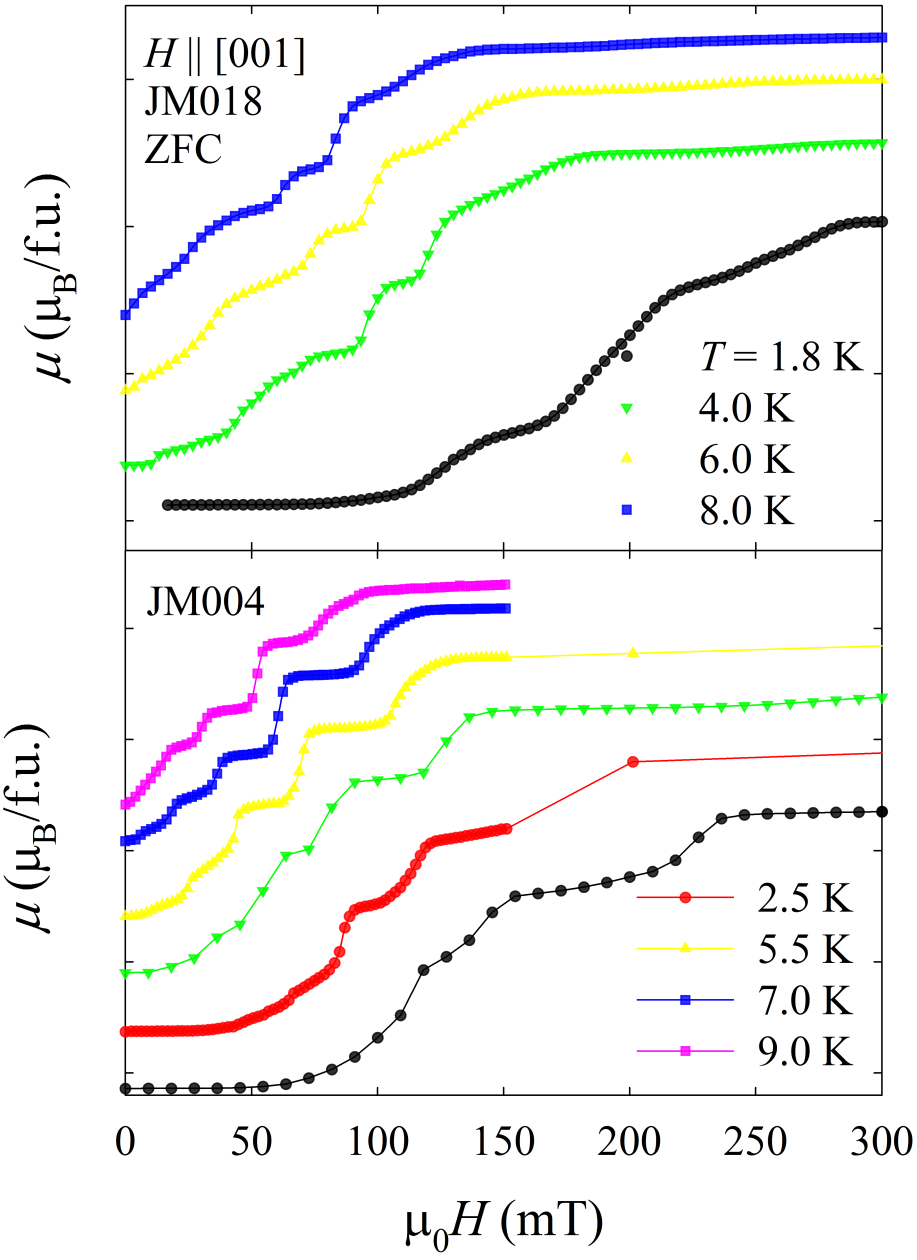

Figure 3.11: Magnetic field dependence of magnetization of $CeCo_{0.715}Si_{2.285}$ at low temperatures and in small magnetic fields applied along [001] direction. The data are displayed without absolute values of magnetization and the curves are scaled on top of each other in order to illustrate the development with temperature.

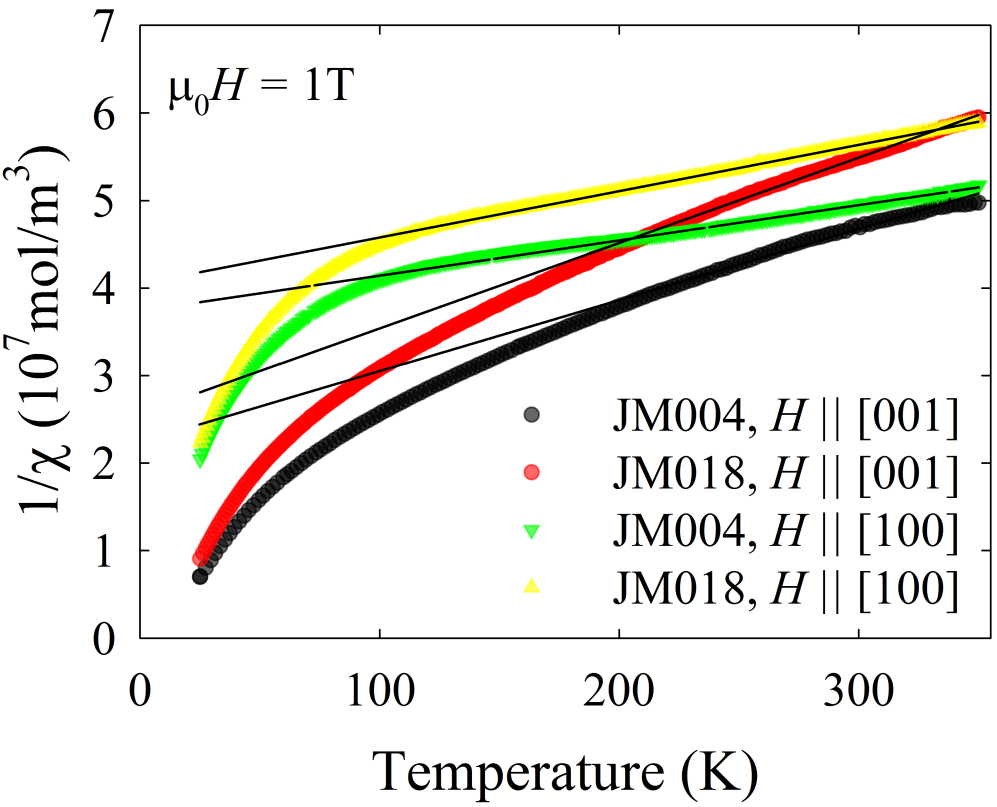

Figure 3.12: Temperature dependence of inverse susceptibility of $CeCo_{0.715}Si_{2.285}$ with magnetic field applied along both [100] and [001] direction, straight lines are linear fits of the Curie-Weiss law in the temperature region 200K $\leq T \leq$ 350K, see Equation 1.2.

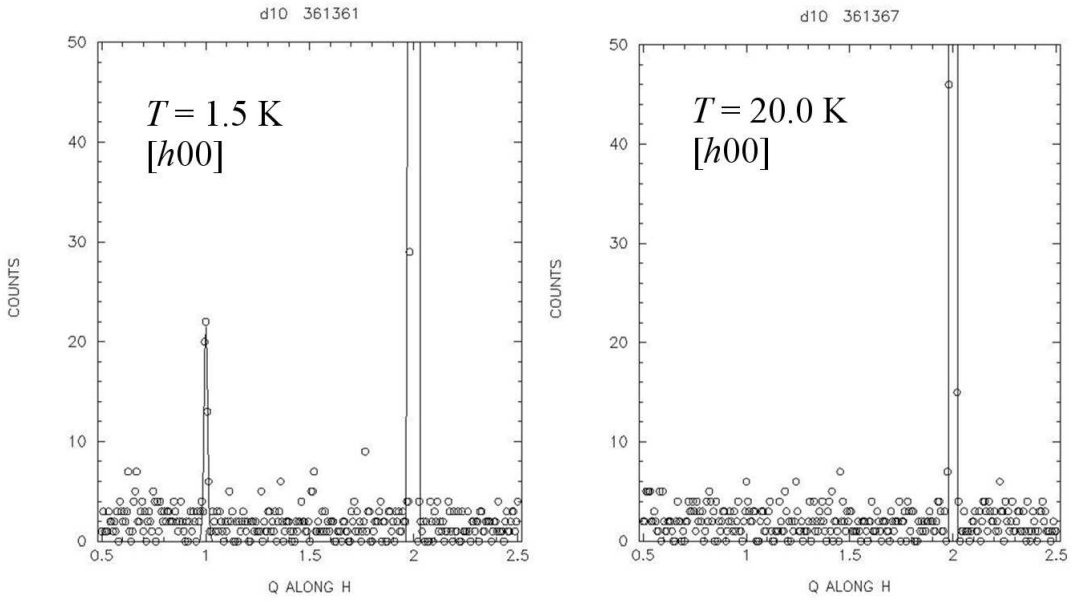

(a) (b)

Figure 3.13: Line scan in reciprocal space along [h00] direction at temperatures (a) $T = 1.5$K and (b) $T = 20$K showing the (100) diffraction at lower temperature.

of magnetic diffractions were much lower than those of the nuclear diffractions. Therefore, if there were any peaks from diffraction on magnetic structure sitting on top of the peaks from diffraction on crystal structure we were unable to determine them. We have, however, been able to observe certain diffraction peaks at positions where the nuclear ones are forbidden by symmetry, such as the (100). It was observed at $T = 1.5$K but not at $T = 20$K, see Figure 3.13, and is obviously of magnetic origin. Another example is the (111) diffraction for which we also measured temperature dependence of intensity. The results are plotted in Figure 3.14 and show that the intensity monotonously decreases and disappears in the background above the ordering temperature $T_{\mathrm{N}} = 10.0$K. We therefore conclude that the crystallographic and magnetic unit cell have the same size and that the probable propagation vectors are $\boldsymbol{k} = (001)$ and $\boldsymbol{k} = (100)$.

As a next step, we performed experiments measuring further diffractions which are forbidden structurally but are present and therefore originate in the magnetic structure. We obtained intensities of the total of 93 diffractions. In order to obtain correct absolute values of the magnetic moments we also performed measurements of nuclear diffractions in the paramagnetic region and obtained intensities of 78 nuclear diffractions. Not all of the diffractions were independent and for further data analysis we first had to calculate intensities of various independent nuclear and magnetic diffractions. For this we used the program DataRed from the FullProf Suite and obtained intensities of 18 and 16 independent diffractions out of the 93 and 78 diffractions measured, respectively. The input files for DataRed were *.col and *.red and the output were *.int and *.out, some of the files we used can be found in Appendix A. The files *.int include the integrated intensities of the measured independent diffractions and are further used as the only experimental data files.

Subsequently, the data obtained in the paramagnetic region containing inten-

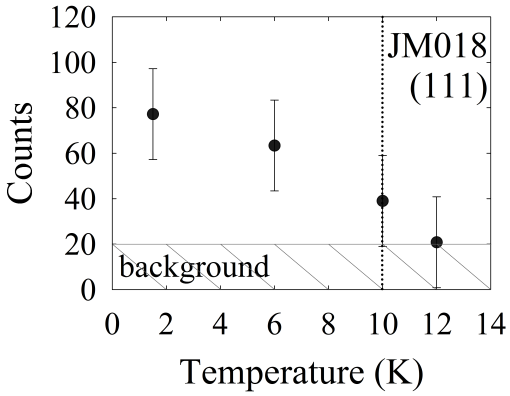

Figure 3.14: Temperature dependence of the intensity of the (111) diffraction including the estimated background. The dotted line shows the ordering temperature $T_{\mathrm{N}} = 10.0\mathrm{K}$.

sities of the nuclear diffractions have been successfully fitted using the Rietveld method, see Section 2.2.2, with the structure obtained from the single X-Ray diffraction experiments, see Section 3.2. The fitted parameters were the fractional coordinates and the new refined values differed from the ones from single crystal X-Ray diffraction by less than 1%.

As a final step, the intensities of magnetic diffractions were fitted. In order to obtain correct values of the magnetic moments the scale factor and structural parameters of such fit must be constrained to have the same values as their nuclear counterpart [47]. Assuming the two propagation vectors $\boldsymbol{k} = (001)$ and $\boldsymbol{k} = (100)$, which we consider the most probable ones, we performed following calculations. It should be stressed that following analysis is only a speculation and some other scenarios are not excluded.

Using the BasIreps program from the FullProf Suite we firstly separated the little group $\mathcal{G}_{\boldsymbol{k}}$ into orthogonal irreducible representations $\mathcal{D}^{(\nu)}$, see Equation 1.27, and then calculated their basis functions $V^{\boldsymbol{k},\nu}_{a,m,j}$, for details see Section 1.2.2. The basis functions for the $\boldsymbol{k} = (001)$ case are summarized in Table 3.3. The BasIreps program uses the procedure provided within the program KAREP [60], the input file for the BasIreps is *.smb, the output files are *.bsr and *.fp, some of the files we used can be found in Appendix B. Using the content of *.fp, i.e. the basis functions $V^{\boldsymbol{k},\nu}_{a,m,j}$, we tried to fit the experimental data via the $C_{a,m}$ coefficients in Equation 1.28 using various combinations of basis functions but were unable to find a solution that would both express the experimental data and be realistic from physical point of view. The lowest R_F agreement factor (24) was obtained for a structure with propagation vector $\boldsymbol{k} = (001)$, Ce(2) moments along c-axis and Ce(3) in basal plane but the size of certain cerium moments was then unrealistically large (three times as much as the free Ce^{3+} ion value of saturated magnetic moment $\mu \simeq 2.14\mu_{\mathrm{B}}$). As mentioned above, we measured magnetic diffraction peaks at positions where the nuclear ones are forbidden by symmetry. This, however, significantly (and systematically) reduced the available reciprocal space. Specifically, for the selected scenario, magnetic diffractions on the Ce(1) site follow the same extinction rules as the nuclear ones and no information about the Ce(1) magnetic moment is present in the acquired data. The results are also summed up in experimental report [61].

$\mathcal{D}^{(\nu)}$	$V^{\boldsymbol{k},\nu}_{a,m,j}$	**Ce1_1**			**Ce2_1**			**Ce2_2**			**Ce3_1**		
		m_x	m_y	m_z	m_x	m_y	m_z	m_x	m_y	m_z	m_x	m_y	m_z
$\mathcal{D}^{(2)}$	$V^{\boldsymbol{k},2}_{1,1,j}$	0	0	1	0	0	1	0	0	-1			
$\mathcal{D}^{(4)}$	$V^{\boldsymbol{k},4}_{1,1,j}$	0	0	1	0	0	1	0	0	1			
$\mathcal{D}^{(5)}$	$V^{\boldsymbol{k},5}_{1,1,j}$	1	1	0	1	0	0	0	1	0	1	-1	0
	$V^{\boldsymbol{k},5}_{1,2,j}$	-1	1	0	0	1	0	1	0	0	-1	-1	0
	$V^{\boldsymbol{k},5}_{2,1,j}$				-1	0	0	0	1	0			
	$V^{\boldsymbol{k},5}_{2,2,j}$				0	1	0	-1	0	0			

Table 3.3: Basis functions $V^{\boldsymbol{k},\nu}_{a,m,j}$ of possible magnetic structures of different cerium sublattices of the studied compound for propagation vector $\boldsymbol{k} = (001)$. Each function is written with the according orthogonal irreducible representation $\mathcal{D}^{(\nu)}$.

4. Discussion

Using the modified Czochralski pulling method, see Section 2.1, we have successfully grown two crystals, labelled JM004 and JM018, of a novel $CeCo_{0.715}Si_{2.285}$ compound and determined its structure. It crystallizes in the *I-4m2* (Nr. 119) space group noncentrosymmetric tetragonal structure with extremely elongated unit cell ($a = b = 4.12$Å and $c = 32.84$Å). The two crystals differ only slightly in Co/Si composition, see Table 3.2, probably on the Co2/Si1D position in the cell, see Table 3.1, and we speculate that there is some region in the ternary phase diagram from which different (but close) compositions can be prepared, depending on the exact initial composition and crystal growth conditions.

Quite interestingly, the $CeCo_{0.715}Si_{2.285}$ structure can be seen as constituting of three building blocks framed by cerium atoms, see Figure 3.2, with the middle block being the $ThCr_2Si_2$ unit cell, see Figure 1, which is derived from the $BaAl_4$ structure and is similar to the $BaNiSn_3$. The $BaNiSn_3$ is a structure of the $CeCoGe_3$ compound which is quite important since (as will be explained later) the magnetic behaviour of $CeCoGe_3$ is similar to the behaviour of the studied $CeCo_{0.715}Si_{2.285}$. The size of the middle block of $CeCo_{0.715}Si_{2.285}$ is $4.12\text{Å} \times 4.12\text{Å} \times 9.46\text{Å}$ which is comparable to the size of the unit cell of $CeCoGe_3$ ($a = 4.319\text{Å}, c = 9.829\text{Å}$ [10]). When looking at the other two building blocks we also see some similarities to the $ThCr_2Si_2$ or $BaNiSn_3$, for example the nearest Si and Co/Si atoms surrounding the Ce(1) atom at (000) position are in similar positions as in $ThCr_2Si_2$ or $BaNiSn_3$ structures.

The compound orders magnetically at $T'_N = 10.7$K and $T_N = 10.0$K for JM004 and JM018 crystal, respectively. The JM004 then undergoes one more successive transition at $T^* = 9.8$K. We interpret this as that the JM018 transits directly to the magnetically ordered ground state while the JM004 transits via some intermediate phase with different magnetic order than the ground state. Both transition are very well visible in the specific heat data, see Figure 3.6. Under application of external magnetic field the transitions are shifted to higher temperatures which is the behaviour usually observed in ferromagnets, we can speculate that the applied field of hundreds of mT is already so large that the compound is no longer in the antiferromagnetically ordered state but already in some field-induced ferromagnetic state. The estimated magnetic entropy gain $\Delta S = 0.14\text{Rln2}$ associated with the transition is quite reduced when compared to the theoretical value which stems from the number of unpaired electrons present in the Ce^{3+} cation $\Delta S_{mag} = \text{Rln}(2s + 1)$, see Equation 1.43. In the temperature region below the ordering temperature the Sommerfeld coefficient (Equation 1.41) has been estimated as $\gamma' = 29\text{mJ/molK}^2$ and $\gamma = 34\text{mJ/molK}^2$ for JM004 and JM018, respectively, the compound is therefore not in a heavy-fermion state. The Sommerfeld coefficient is comparable to the value reported for $CeCoGe_3$, $\gamma_{CeCoGe_3} = 32\text{mJ/molK}^2$, the entropy gain, however, is much smaller, $\Delta S_{CeCoGe_3} = 0.68\text{ln2}$ [10]. We attribute the low value of the magnetic entropy gain to a significant reduction of the cerium magnetic moment (in comparison to the free Ce^{3+} ion value) which will be discussed later.

The temperature dependence of electrical resistivity, see Figure 3.7, exhibits behaviour similar to the one of $CeCoGe_3$ – it remains almost unchanged from

room temperature down to temperatures around 150 K and then decreases steeply. In the case of JM018 crystal the magnetic ordering temperature $T_N = 10.0$K is clearly marked by a change of slope of resistivity and the dependency is isotropic. The absolute values of resistivity for $J||[001]$ are about three times higher than for $J||[100]$. This is quite interesting and as a possible explanation we may consider the following scenario: the JM018 samples were not annealed and the transport properties therefore see a certain difference in Co/Si occupation in various layers along c direction whereas in a direction the structure is homogeneous. This scenario is, however, highly speculative.

The first pressure experiments revealed that the magnetic ordering is suppressed by application of external pressure, see Figure 3.8. The ordering temperature T'_N is gradually lowered and we speculate that at pressures around 6–7GPa the magnetic order might be suppressed completely and superconducting ground state might appear (as is quite common in cerium-based ternaries). Since the observed behaviour is very interesting, the development of T'_N under higher pressures is being further investigated by J. Valenta within the course of his PhD thesis.

Below the ordering temperature in external magnetic field the magnetization of the studied compound $CeCo_{0.715}Si_{2.285}$ exhibits the step-like behaviour similar to the behavior of the so-called 'devil's staircase' systems (e.g. CeSb [9], $CeRh_3Si_2$ [62], $CeCoGe_3$ [10], etc.). At fields of 1T the magnetization is more or less saturated and increases only slightly linearly with field $H||[001]$ up to 45T. When the field is applied in basal direction (along the hard magnetization axis) the magnetization increases very slowly linearly and exhibits none of the low-field step-like behaviour observed in $H||[001]$ experiments, see Figure 3.10. Such uniaxial anisotropy is observed in the $CeCoGe_3$ as well and in this compound it stems from the anisotropic magnetic structure with moments oriented along the [001] direction, see Figure 4.2. The hard axis magnetization above 7T increases quite steeply and non-linearly and at field of 35T equals to the easy axis magnetization. Concerning the absolute size of the magnetization its saturated value at 1T is considerably reduced – $0.26\mu_B$/Ce for JM004 and $0.21\mu_B$/Ce for JM018 – with respect to the free Ce^{3+} ion value of saturated magnetic moment $\mu \simeq 2.14\mu_B$, see Equation 1.5. The reduction of magnetic moment size is quite common in Ce-based ternary intermetallics but usually magnetic moment of around $1.0\mu_B$ is observed. Here the magnetic moment reduction is more significant and, as in the case of $CeCoGe_3$ [63] in which ordered moment of around $0.4\mu_B$ is observed, we attribute it to hybridization between localized Ce^{3+} f electrons and the conduction band. The studied compound also shows a ferromagnet-like magnetization curve with strong hysteresis and remanent magnetization only marginally reduced with respect to saturated magnetization. It also exhibits hysteresis with respect to varying temperature, see Figure 3.9.

As shown in Figure 3.12 at high temperatures, $200\text{K} \leq T \leq 350\text{K}$, temperature dependence of magnetic susceptibility of $CeCo_{0.715}Si_{2.285}$ can be fitted by the Curie-Weiss law, see Equation 1.2. A small but non-negligible deviation of the data is observed at high temperatures with field $H||[001]$ for JM004 crystal. Results of the least-squares fit of the Curie-Weiss law, the effective magnetic moments and paramagnetic Curie-Weiss temperatures, are summed up below in Table 4.1 for fields applied both along a- and c-axis. The values of effective moments are as

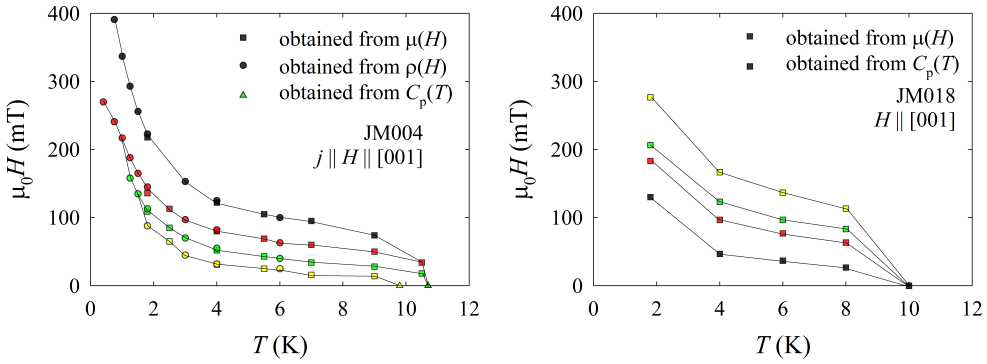

(a) (b)

Figure 4.1: Magnetic phase diagram of $CeCo_{0.715}Si_{2.285}$ crystals (a) JM004 and (b) JM018 based on experiments measuring the temperature dependence of specific heat $C_p(T)$ and field dependencies of magnetization $\mu(H)$ and electrical resistivity $\rho(H)$.

large as $3.97\mu_B$ and in comparison to the value of effective magnetic moment of the free Ce^{3+} ion $\mu_{eff} \simeq 2.54\mu_B$, see Equation 1.5, are unrealistic. The behaviour of the compound thus can not be described using the Curie-Weiss model. Still, the large negative values of the paramagnetic Curie-Weiss temperature θ_p show predominance of antiferromagnetic interactions.

The most interesting feature of the studied compound, however, is the above mentioned step-like behaviour of magnetization, i.e. the successive metamagnetic transitions, in small fields $\mu_0 H < 0.5$T applied along the c-axis. Below the temperature of 11.0K firstly two phase transitions appear at 34mT and 18mT (for JM004), further on, with decreasing temperature the transitions shift to higher magnetic fields and new transitions appear. At temperatures below 2.5K the number of transitions is again reduced while still being shifted to higher magnetic fields. As shown in Figure 3.10 the numerous magnetic phase transitions are also manifested in magnetic field dependence of electrical resistivity, however, the step-like behaviour is more pronounced in the magnetization data. Based on the experiments measuring the temperature dependence of specific heat and field dependencies of magnetization and electrical resistivity we constructed a magnetic phase diagram, see Figure 4.1, in a similar fashion to the one of the CeSb in Figure 4.

The above–described magnetic behaviour suggests a series of consequent magnetic structures with increasing field, such as the ones in $CeCoGe_3$ [63] or CeSb which are described by a periodic stacking of zero magnetized and ferromagnetic planes with parallel or antiparallel magnetization. For CeSb they are at low temperatures described with propagation vectors $k = 4/7(++--++-)$, $k = 2/3(++-)$ and $k = 0$ [24]. The next logical step therefore was to investigate the magnetic structure of the studied compound with appropriate experiments which in our case was the neutron diffraction.

Neutron diffraction experiments were performed at ILL on single-crystal four-circle diffractometer with three-axis energy analysis (D10). The experiments confirmed good crystallinity of the sample and confirmed the structure determined from the X-Ray diffraction experiments. In paramagnetic and ordered state, we

were able to obtain 93 (18 independent) nuclear and 78 (16) magnetic diffractions, respectively. The temperature dependence of (111) diffraction, see Figure 3.14, showed agreement of the diffraction experiments with magnetic ordering observed in bulk properties at $T_N = 10.0$K.

From experiments at low temperatures first observations about the magnetic structure were made. Firstly, the magnetic unit cell has the same size as the crystal one and possible propagation vectors are $\boldsymbol{k} = (001)$ and $\boldsymbol{k} = (100)$. Secondly, the size of the cerium moments is very much reduced (which is an assumption already made based on measurements of magnetization) and therefore so is the intensity of diffractions on the periodic magnetic structure. This complicates the magnetic structure determination since only the magnetic diffractions on positions where the nuclear ones are forbidden by symmetry, such as the (100) in Figure 3.13, could have been measured (due to the very high but still not sufficient precision of the experiment). This in turn significantly (and systematically) reduced the size of the explored reciprocal space and if the propagation vector was truly $\boldsymbol{k} = (001)$ also caused that no information about the Ce(1) magnetic moments is present in our experimental data.

The lowest R_F agreement factor (24) was obtained for a structure with propagation vector $\boldsymbol{k} = (001)$ and Ce(2) moments along c-axis and Ce(3) in basal plane. However, the size of certain cerium moments was then unrealistically large and this scenario is also in contrast to the usual magnetic structure of similarly behaving cerium compounds, such as the $CeCoGe_3$, see Figure 4.2.

The described neutron experiment was an initial one and did not give any definite conclusion about magnetic structure of the studied $CeCo_{0.715}Si_{2.285}$. It proposes a few scenarios and further investigation is necessary. A continuation proposal for further single crystal neutron diffraction experiments has already been submitted.

All of the above–described properties of JM004 and JM018 crystals are summed up in Table 4.1.

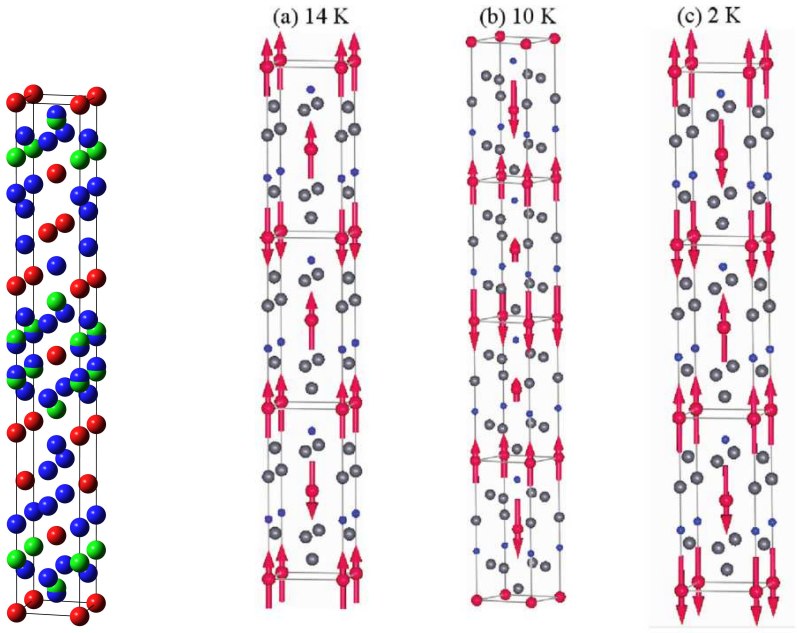

(a) (b)

Figure 4.2: (a) Structure of $CeCo_{0.715}Si_{2.285}$ as determined by I. Císařová, (b) magnetic structure of $CeCoGe_3$ at $T = 14K$, $10K$ and 2K as determined in Ref. [63]. Cerium atoms are displayed in red.

property	**JM004**	**JM018**
Ce/Co/Si content	26.0 / 21.5 / 52.5 %	24.4 / 17.6 / 58.0 %
T_{ord}	10.7 / 9.8 K	10.0 K
γ	29mJ/molK^2	34mJ/molK^2
ΔS	0.14Rln2	0.14Rln2
μ_{S} in 1T	$0.26\mu_{\mathrm{B}}$/Ce	$0.21\mu_{\mathrm{B}}$/Ce
$\mu_{\mathrm{eff}}^{\|\|c}$	$2.8\mu_{\mathrm{B}}$/Ce	$2.55\mu_{\mathrm{B}}$/Ce
$\theta_{\mathrm{p}}^{\|\|c}$	-276K	-263K
$\mu_{\mathrm{eff}}^{\|\|a}$	$3.97\mu_{\mathrm{B}}$/Ce	$3.47\mu_{\mathrm{B}}$/Ce
$\theta_{\mathrm{p}}^{\|\|a}$	-928K	-766K

Table 4.1: Sum of physical properties of JM004 and JM018 crystals of $CeCo_{0.715}Si_{2.285}$.

Conclusion and Outlook

Using modified Czochralski pulling method we have successfully grown single crystals of a novel $CeCo_{0.715}Si_{2.285}$ compound and characterised its crystallographic structure, thermodynamic, transport and magnetic properties and performed first experiments studying its magnetic structure. The compound exhibits some interesting magnetic behaviour similar to a (structurally-close) $CeCoGe_3$ which probably stems from a quite uncommon magnetic structure.

The compound crystallizes in the *I-4m2* space group structure with extremely elongated unit cell ($a = 4.13$Å , $c = 32.84$Å) containing $BaAl_4$ structural patterns including a complete $ThCr_2Si_2$ unit cell. In zero magnetic field it orders antiferromagnetically at $T_N = 10.0$K, the change of magnetic entropy connected to this ordering is $\Delta S = 0.14$Rln2. The Sommerfeld coefficient at low temperatures has been estimated as $\gamma = 34\text{mJ/molK}^2$. The magnetic ordering is clearly observed in specific heat, resistivity and magnetization data.

The magnetization of the compound is anisotropic and at low temperatures the compound exhibits a ferromagnet-like magnetization curve with strong hysteresis and remanent magnetization only marginally reduced with respect to saturated magnetization. It also exhibits hysteresis with respect to varying temperature. Under application of small magnetic fields ($B < 0.5$T) along the c-axis it manifests numerous magnetic transitions resembling the so-called 'devil's staircase' behaviour (e.g. CeSb, $CeCoGe_3$). With decreasing temperature the transitions shift to higher magnetic fields, at temperatures below 2.5K the number of transitions is reduced while still being shifted the same way. Based on the experiments measuring the temperature dependence of specific heat and field dependencies of magnetization and electrical resistivity a magnetic phase diagram has been constructed.

At high fields applied along the c-axis the magnetization remains almost constant and increases only slightly linearly in fields up to 45T. The saturated value of magnetization at 1T is considerably reduced ($0.21\mu_B$/Ce) with respect to the free Ce^{3+} ion value of saturated magnetic moment. For fields applied along the a-axis typical behaviour for the hard axis in a material with uniaxial anisotropy is observed. At high temperatures the inverse susceptibility is linear with temperature, however, the behaviour can not be described using the Curie-Weiss model.

Results of first single crystal neutron diffraction experiments indicate that the magnetic unit cell has the same size as the crystal one and possible propagation vectors are $\boldsymbol{k} = (001)$ and $\boldsymbol{k} = (100)$. However, due to a significantly reduced size of the cerium moments the magnetic structure experiments are quite complicated and further measurements need to be performed before conclusions about the magnetic structure can be made.

In the future, further development of the compound's ordering temperature with applied external pressure will be studied together with the possibility of a superconducting ground state emergence. Also a continuation proposal for further single crystal neutron diffraction experiments has been submitted in order to clarify the magnetic order behind the curious behaviour of $CeCo_{0.715}Si_{2.285}$.

Bibliography

[1] "The Nobel Prize in Physics 2007 to Albert Fert and Peter Grunberg 'for the discovery of Giant Magnetoresistance'." `http://www.nobelprize.org/nobel_prizes/physics/laureates/2007`, April 2015.

[2] Y. Onuki, R. Settai, K. Sugiyama, T. Takeuchi, T. C. Kobayashi, Y. Haga, and E. Yamamoto, "Recent advances in the magnetism and superconductivity of heavy fermion systems," *Journal of the Physical Society of Japan*, vol. 73, no. 4, pp. 769–787, 2004.

[3] G. Riblet and K. Winzer, "Vanishing of superconductivity below a second transition temperature in (La1-xCex)Al2 alloys due to the kondo effect," *Solid State Communications*, vol. 9, pp. 1663–1665, 1971.

[4] M. B. Maple, W. A. Fertig, A. C. Mota, L. E. DeLong, D. Wohlleben, and R. Fitzgerald, "The re-entrant superconducting-normal phase boundary of the Kondo system (La,Ce)Al2," *Solid State Communications*, vol. 11, pp. 829–834, 1972.

[5] N. E. Phillips and B. T. Matthias, "Heat capacity of ferromagnetic superconductors," *Physical Review*, vol. 121, pp. 105–107, 1961.

[6] F. Steglich, J. Aarts, C. D. Bredl, W. Lieke, D. Meschede, W. Franz, and H. Schaefer, "CeCu2Si2," *Physical Review Letters*, vol. 43, no. 25, pp. 1892–1896, 1979.

[7] C. Pfleiderer, "Superconducting phases of f-electron compounds," *Reviews of Modern Physics*, vol. 81, no. November, 2009.

[8] J. Moudřík, J. Prokleška, J. Pospíšil, V. Sechovský, and I. Císařová, "Magnetic Properties of a Novel CeCo0.715Si2.285 Compound," *Acta Physica Polonica A*, vol. 127, no. 2, pp. 561–563, 2015.

[9] J. Rossat-Mignod, J. M. Effantin, P. Burlet, T. Chattopadhyay, and L. P. Regnault, "Neutron and Magnetization Studies of CeSb and CeSb1-xTex Solid Solutions," *Journal of Magnetism and Magnetic Materials*, vol. 52, pp. 111–121, 1985.

[10] A. Thamizhavel, T. Takeuchi, T. D. Matsuda, Y. Haga, K. Sugiyama, R. Settai, and Y. Onuki, "Unique Magnetic Phases in an Antiferromagnet CeCoGe3," *Journal of the Physical Society of Japan*, vol. 74, pp. 1858–1864, June 2005.

[11] N. Kimura, K. Ito, K. Saitoh, Y. Umeda, H. Aoki, and T. Terashima, "Pressure-Induced Superconductivity in Noncentrosymmetric Heavy-Fermion CeRhSi3," *Physical Review Letters*, vol. 95, p. 247004, Dec. 2005.

[12] R. Movshovich, T. Graf, D. Mandrus, J. Thompson, J. Smith, and Z. Fisk, "Superconductivity in heavy-fermion CeRh2Si2.," *Physical Review B*, vol. 53, pp. 8241–8244, Apr. 1996.

[13] I. Sugitani, Y. Okuda, H. Shishido, T. Yamada, A. Thamizhavel, E. Yamamoto, T. D. Matsuda, Y. Haga, T. Takeuchi, R. Settai, and Y. Onuki, "Pressure-Induced Heavy-Fermion Superconductivity in Antiferromagnet CeIrSi3 without Inversion Symmetry," *Journal of the Physical Society of Japan*, vol. 75, p. 043703, Apr. 2006.

[14] R. Settai, Y. Okuda, I. Sugitani, Y. Onuki, T. D. Matsuda, Y. Haga, and H. Harima, "Non-centrosymmetric heavy fermion superconductivity in CeCoGe3," *International Journal of Modern Physics B*, vol. 21, no. 18-19, pp. 3238–3245, 2007.

[15] F. Honda, I. Bonalde, K. Shimizu, S. Yoshiuchi, Y. Hirose, T. Nakamura, R. Settai, and Y. Onuki, "Pressure-induced superconductivity and large upper critical field in the noncentrosymmetric antiferromagnet CeIrGe3," *Physical Review B*, vol. 81, p. 140507, Apr. 2010.

[16] Y. Okuda, Y. Miyauchi, Y. Ida, Y. Takeda, C. Tonohiro, Y. Oduchi, T. Yamada, N. D. Dung, T. D. Matsuda, Y. Haga, T. Takeuchi, M. Hagiwara, K. Kindo, H. Harima, K. Sugiyama, R. Settai, and Y. Onuki, "Magnetic and Superconducting Properties of LaIrSi3 and CeIrSi3 with the Noncentrosymmetric Crystal Structure," *Journal of the Physical Society of Japan*, vol. 76, p. 044708, Apr. 2007.

[17] G. Eguchi, D. C. Peets, M. Kriener, Y. Maeno, E. Nishibori, Y. Kumazawa, K. Banno, S. Maki, and H. Sawa, "Crystallographic and superconducting properties of the fully gapped noncentrosymmetric 5d-electron superconductors CaMSi3 (M= Ir, Pt)," *Physical Review B*, vol. 83, p. 024512, 2011.

[18] M. Smidman, A. D. Hillier, D. T. Adroja, M. R. Lees, V. K. Anand, R. P. Singh, R. I. Smith, D. M. Paul, and G. Balakrishnan, "Investigations of the superconducting states of noncentrosymmetric LaPdSi3 and LaPtSi3," *Physical Review B*, vol. 89, p. 094509, 2014.

[19] N. Kimura and I. Bonalde, "Non-Centrosymmetric Heavy-Fermion Superconductors," in *"Non-Centrosymmetric Superconductors: Introduction and Overview", Lecture Notes in Physics 847*, pp. 35–79, Jan. 2012.

[20] J. Moudřík, "Study of magnetic behaviour in CeTX3 compounds," *Bachelor thesis, Charles University in Prague*, 2013.

[21] D. Eom, M. Ishikawa, J. Kitagawa, and N. Takeda, "Suppression of Antiferromagnetism by Kondo Effect and Quantum Critical Behavior in CeCoGe3-xSix," *Journal of the Physical Society of Japan*, vol. 67, no. 7, pp. 2495–2500, 1998.

[22] Y. Muro, D. Eom, N. Takeda, and M. Ishikawa, "Contrasting Kondo-Lattice Behavior in CeTSi3 and CeTGe3 (T=Rh and Ir)," *Journal of the Physical Society of Japan*, vol. 67, no. 10, pp. 3601–3604, 1998.

[23] T. Kawai, H. Muranaka, M.-A. Measson, T. Shimoda, Y. Doi, T. D. Matsuda, Y. Haga, G. Knebel, G. Lapertot, D. Aoki, J. Flouquet, T. Takeuchi, R. Settai, and Y. Onuki, "Magnetic and Superconducting Properties of

CeTX3 (T: Transition Metal and X: Si and Ge) with Non-centrosymmetric Crystal Structure," *Journal of the Physical Society of Japan*, vol. 77, p. 064716, June 2008.

[24] J. Rossat-Mignod, P. Burlett, J. Villain, H. Bartholint, W. Tcheng-Si, D. Florence, and O. Vogt, "Phase diagram and magnetic structures of CeSb," *Physical Review B*, vol. 16, no. 1, pp. 440 – 461, 1977.

[25] P. J. Mohr, B. N. Taylor, and D. B. Newell, "CODATA recommended values of the fundamental physical constants: 2010," *Reviews of Modern Physics*, vol. 84, no. December, pp. 1527–1605, 2012.

[26] C. Kittel, *Introduction to Solid State Physics, 8th edition.* John Wiley & Sons, Inc, 2005.

[27] R. P. Feynman, R. B. Leighton, and M. Sands, *The Feynman Lectures on Physics Vol. 3.* Addison-Wesley Publishing Company, Inc., 1964.

[28] J. Kubler, *Theory of Itinerant Electron Magnetism.* Oxford University Press, 2000.

[29] E. C. Stoner, "Collective Electron Ferromagnetism," *Proceedings of the Royal Society of London A: Mathematical, Physical and Engineering Sciences*, vol. 165, no. 922, pp. 372–414, 1938.

[30] E. C. Stoner, "Collective Electron Ferromagnetism. II. Energy and Specific Heat," *Proceedings of the Royal Society of London A: Mathematical, Physical and Engineering Sciences*, vol. 169, no. 938, pp. 339–371, 1939.

[31] K. Yosida, *Theory of Magnetism.* Springer, 1996.

[32] M. A. Ruderman and C. Kittel, "Indirect exchange coupling of nuclear magnetic moments by conduction electrons," *Physical Review*, vol. 96, no. 3, pp. 99–102, 1954.

[33] T. Kasuya, " A Theory of Metallic Ferro- and Antiferromagnetism on Zener's Model ," *Progress of Theoretical Physics*, vol. 16, no. 1, pp. 45–57, 1956.

[34] K. Yosida, "Magnetic properties of Cu-Mn alloys," *Physical Review*, vol. 106, no. I, 1957.

[35] J. Kondo, "Resistance Minimum in Dilute Magnetic Alloys," *Progress of Theoretical Physics*, vol. 32, no. 1, pp. 37–49, 1964.

[36] F. C. Schwerer, J. W. Conroy, and S. Arajs, "Matthiessen's rule and the electrical resistivity of iron-silicon solid solutions," *Journal of Physics and Chemistry of Solids*, vol. 30, pp. 1513–1525, 1969.

[37] V. Valvoda, M. Polcarová, and P. Lukáč, *Základy Strukturní Analýzy.* Karolinum, 1992.

[38] J. W. Goodman, *Introduction to Fourier optics.* Roberts and Company Publishers, 2005.

[39] A. Wills, "Magnetic structures and their determination using group theory," *Le Journal de Physique IV*, vol. 11, pp. Pr9–133–Pr9–158, 2001.

[40] J. Rodriguez-Carvajal, "Recent advances in magnetic structure determination by neutron powder diffraction," *Physica B*, vol. 192, pp. 55–69, 1993.

[41] K. Huang, *Statistical Mechanics*. John Wiley & Sons, Inc, 1987.

[42] C. A. Martin, "Simple treatment of anharmonic effects on the specific heat," *Journal of Physics: Condensed Matter*, vol. 3, pp. 5967–5974, 1991.

[43] S. E. Ziemniak, L. M. Anovitz, R. a. Castelli, and W. D. Porter, "Magnetic contribution to heat capacity and entropy of nickel ferrite (NiFe2O4)," *Journal of Physics and Chemistry of Solids*, vol. 68, pp. 10–21, 2007.

[44] J. Czochralski, "Ein neues Verfahren zur Messung der Kristallisationsgeschwindigkeit der Metalle.," *Zeitschrift fuer Physikalische Chemie*, vol. 92, pp. 219–221, 1918.

[45] N. W. Ashcroft and N. D. Mermin, *Solid State Physics*. 1976.

[46] "The X-Ray Group, Department of Condensed Matter Physics of Charles University." `http://xray.cz/kfkl-osa/eng/osainst.htm`, April 2013.

[47] "FullProf Suite." `http://www.ill.eu/sites/fullprof/`, February 2015.

[48] H. M. Rietveld, "Line profiles of neutron powder-diffraction peaks for structure refinement," *Acta Crystallographica*, vol. 22, pp. 151–152, 1967.

[49] H. M. Rietveld, "A profile refinement method for nuclear and magnetic structures," *Journal of Applied Crystallography*, vol. 2, pp. 65–71, 1969.

[50] "D10 - Four-circle diffractometer with three-axis energy analysis." url: http://www.ill.eu/en/html/instruments-support/instruments-groups/instruments/d10/description/instrument-layout/, February 2015.

[51] "Joint Laboratory for Magnetic Studies, Department of Condensed Matter Physics of Charles University." `http://kfkl.cz/jlms/`, April 2013.

[52] "Physical Property Measurement System, Quantum Design." `http://www.qdusa.com/products/ppms.html`, April 2013.

[53] Quantum Design, *Physical Property Measurement System, Heat Capacity Option User's Manual*. No. 1085-150, 2004.

[54] J. S. Hwang, K. J. Lin, and C. Tien, "Measurement of heat capacity by fitting the whole temperature response of a heat-pulse calorimeter," *Review of Scientific Instruments*, vol. 68, no. 1997, p. 94, 1997.

[55] J. C. Lashley, M. F. Hundley, a. Migliori, J. L. Sarrao, P. G. Pagliuso, T. W. Darling, M. Jaime, J. C. Cooley, W. L. Hults, L. Morales, D. J. Thoma, J. L. Smith, J. Boerio-Goates, B. F. Woodfield, G. R. Stewart, R. a. Fisher, and N. E. Phillips, "Critical examination of heat capacity measurements made on a quantum design physical property measurement system," *Cryogenics*, vol. 43, pp. 369–378, 2003.

[56] "Magnetism and Low Temperature Laboratories." `http://lmnt.cz/`, March 2015.

[57] J. Clarke and A. I. Braginski, eds., *The SQUID Handbook*. WILEY-VCH Verlag GmbH and Co. KGaA, 2004.

[58] "Technology Lab, Department of Condensed Matter Physics of Charles University." `http://kfkl.cz/techlab/`, April 2013.

[59] D. Fort, "The purification and crystal growth of rare earth metals using solid state electrotransport," *Journal of the Less-Common Metals*, vol. 134, pp. 45–65, 1987.

[60] E. Hovestreydt, M. Aroyo, S. Sattler, and H. Wondratschek, "KAREP - a program for calculating irreducible space-group representations," *Journal of Applied Crystallography*, vol. 25, no. May, pp. 544–544, 1992.

[61] "Experimental report nr. 5-41-771," *D10, From : 26/11/2014 To : 02/12/2014*.

[62] D. Kaczorowski and T. Komatsubara, "Complex magnetic behavior in single-crystalline CeRh3Si2," *Physica B: Condensed Matter*, vol. 403, pp. 1362–1364, Apr. 2008.

[63] M. Smidman, D. T. Adroja, a. D. Hillier, L. C. Chapon, J. W. Taylor, V. K. Anand, R. P. Singh, M. R. Lees, E. a. Goremychkin, M. M. Koza, V. V. Krishnamurthy, D. M. Paul, and G. Balakrishnan, "Neutron scattering and muon spin relaxation measurements of the noncentrosymmetric antiferromagnet CeCoGe3," *Physical Review B*, vol. 88, p. 134416, 2013.

List of Tables

A. DataRed Input and Output Files

refl_nucl.col (first 10 lines)

```
361409  2.000  0.000  8.000    141.27     26.45   39.95   39.95   25.25 -140.60   1.73
361410  2.000  0.000  6.000     61.67     16.40   37.84   37.84   27.28 -134.31   1.73
361412  2.000  0.000  2.000     38.78     17.69   35.39   35.39   30.72 -119.50   1.75
361413  2.000  0.000  0.000  29653.53    356.81   35.08   35.08   31.83 -111.29   1.72
361414  2.000  0.000 -2.000     27.59     22.33   35.39   35.39   32.42 -102.92   1.75
361415  2.000  0.000 -4.000     36.17     15.46   36.32   36.32   32.45  -94.76   1.76
361416  2.000  0.000 -6.000     42.14     15.70   37.84   37.84   32.00  -87.09   1.73
361417  2.000  0.000 -8.000    135.99     26.35   39.95   39.95   31.18  -80.11   1.73
361422 -1.000  1.000 -6.000  11025.28    193.50   27.36   27.36   14.20   45.07   1.72
361424 -1.000  1.000 -4.000    262.14     39.69   25.52   25.52   14.16   53.78   1.72
```

refl_nucl.red

```
TITLE CeCoSi
INPFIL refl_nucl.col
OUTFIL refl_nucl
CELL     4.130000    4.130000   32.840000     90.0000     90.0000     90.0000
SPGR I -4 m 2
WAVE      2.36000
HKL_T    5
SCALE    1.000
```

refl_nucl.int

```
TITLE
CeCoSi
(3i4,2F14.4,i5,4f8.2)
2.36000   0   0
0   0   2        7.6916        2.6950    1    8.24    4.11   -5.86  162.37
0   0   4       11.7384        3.8900    1   16.53    8.23    5.86  -17.63
0   0   6       50.9423        9.8650    1   24.90   12.41   -5.86  162.37
0   0   8       83.5953       14.6250    1   33.41   16.65    5.86  -17.63
1   0   1       31.4622       14.5199    1   33.47   16.83   58.16   68.34
1   0   3       18.4299       11.4123    1   35.56   17.86   48.96  113.22
1   0   5       54.2446       14.5487    1   39.45   19.79   41.44  125.48
1   0   7      136.8606       21.4250    1   44.75   22.41   27.69  -63.81
1   1   0       66.6853       23.6900    1   47.66   23.98   12.91   73.72
1   1   2      297.5119      105.3352    1   48.46   24.37   76.50  -88.99
1   1   4      317.0970      106.2099    1   50.79   25.52   14.16   53.78
1   1   6    11274.9111     1090.6001    1   54.51   27.36   54.02 -177.88
1   1   8      762.9315      119.9152    1   59.46   29.81   58.34  -38.10
2   0   0    25368.4180     2724.6064    1   69.70   35.08   31.83 -111.29
2   0   2       24.5416       17.5967    1   70.33   35.39   30.72 -119.50
2   0   4       18.9622       11.8880    1   72.20   36.32   57.47   55.45
2   0   6       47.2782       18.7100    1   75.29   37.84   32.00  -87.09
2   0   8      150.5829       27.3817    1   79.53   39.95   45.17  120.06
```

B. BasIreps Input and Output Files

cecosi_mag.smb

```
TITLE CeCoSi
SPGR  I -4 m 2
KVEC   0.0000  0.0000  1.0000 X
BASIR AXIAL CEL
ATOM Ce1  Ce1   0.00000  0.00000  0.00000
ATOM Ce2  Ce2   0.00000  0.00000  0.64610
ATOM Ce3  Ce3   0.00000  0.50000  0.25000
```

cecosi_mag.fp (first 36 lines)

```
-------------------------------
Output of BasIREPS for FullProf
-------------------------------
The group of lines starting with the symbol of space groups and
finishing with the last keyword BASI, may be pasted into the PCR file


=> Basis functions of Representation IRrep( 4) of dimension  1 contained 1 times in GAMMA
Representation number    :  4 for Site:  1
Number of basis functions:  1

----- Block-of-lines for PCR start just below this line
I -1                          <--Space group symbol for hkl generation
! Nsym   Cen  Laue Ireps N_Bas
1     1     1    -1     1
! Real(0)-Imaginary(1) indicator for Ci
0
SYMM x,y,z
BASR   0  0  1
BASI   0  0  0
----- End-of-block of lines for PCR

=> Basis functions of Representation IRrep( 5) of dimension  2 contained 1 times in GAMMA
Representation number    :  5 for Site:  1
Number of basis functions:  2

----- Block-of-lines for PCR start just below this line
I -1                          <--Space group symbol for hkl generation
! Nsym   Cen  Laue Ireps N_Bas
1     1     1    -1     2
! Real(0)-Imaginary(1) indicator for Ci
0  0
SYMM x,y,z
BASR   1  1  0  -1  1  0
BASI   0  0  0   0  0  0
----- End-of-block of lines for PCR
```